Journal of the Mechanics and Physics of Solids
52 (2004) 1213 – 1246

JOURNAL OF THE
MECHANICS AND
PHYSICS OF SOLIDS

www.elsevier.com/locate/jmps

On the evolution of crystallographic dislocation density in non-homogeneously deforming crystals

Athanasios Arsenlis[a,*], David M. Parks[b], Richard Becker[a],
Vasily V. Bulatov[a]

[a]Lawrence Livermore National Laboratory, University of California, P.O. Box 808,
L-371, Livermore, CA 94551, USA
[b]Department of Mechanical Engineering, Massachusetts Institute of Technology,
77 Massachusetts Avenue, Cambridge, MA 02139, USA

Received 23 April 2003; received in revised form 13 December 2003; accepted 17 December 2003

Abstract

A set of evolution equations for dislocation density is developed incorporating the combined evolution of statistically stored and geometrically necessary densities. The statistical density evolves through Burgers vector-conserving reactions based in dislocation mechanics. The geometric density evolves due to the divergence of dislocation fluxes associated with the inhomogeneous nature of plasticity in crystals. Integration of the density-based model requires additional dislocation density/density-flux boundary conditions to complement the standard traction/displacement boundary conditions. The dislocation density evolution equations and the coupling of the dislocation density flux to the slip deformation in a continuum crystal plasticity model are incorporated into a finite element model. Simulations of an idealized crystal with a simplified slip geometry are conducted to demonstrate the length scale-dependence of the mechanical behavior of the constitutive model. The model formulation and simulation results have direct implications on the ability to explicitly model the interaction of dislocation densities with grain boundaries and on the net effect of grain boundaries on the macroscopic mechanical response of polycrystals.

Keywords: Crystal plasticity; Strain gradient plasticity; Continuum dislocation theory

---

[*] Corresponding author. Tel.: +1-925-424-2584; fax: +1-925-423-7040.
E-mail address: arsenlis@llnl.gov (A. Arsenlis).

0022-5096/$ - see front matter © 2003 Elsevier Ltd. All rights reserved.
doi:10.1016/j.jmps.2003.12.007

1. Introduction

Crystal plasticity is an inherently non-homogeneous process. The deformation of polycrystalline metals may appear macroscopically homogeneous; however, each crystal in the aggregate undergoes a different mode of deformation that, tensorially averaged with the rest of the grains, leads to the macroscopic deformation mode observed. Experimental observations using Orientation Imaging Microscopy (OIM) have shown the level of inhomogeneity in the plastic deformation between neighboring grains (Sun et al., 2000). Theoretical investigations of polycrystals have attempted to show how the inhomogeneity of the plastic deformation between neighboring grains may be responsible for the grain-size dependence (i.e. Hall–Petch) of flow stress (Smyshlyaev and Fleck, 1996; Dai and Parks, 1997; Acharya and Beaudoin, 2000).

Non-homogeneous plastic deformation is not limited to polycrystals, but is also found within single crystals at smaller length scales. Slip trace analysis of plastically deformed single crystals shows regions of “patchy” slip forming when the loading direction coincides with a high-symmetry axis of the crystal. In these highly symmetric orientations, multiple slip-systems are potentially active; however, all of the slip-systems with equally large resolved shear stresses do not contribute equally to the plastic deformation at microscopic length scales (Kocks, 1959). More recently, OIM measurements of a Ta single crystal deformed with the [1 1 0]-crystallographic direction parallel to the tensile loading axis have shown that the orientation of the crystal oscillates, locally, and that the wavelength of orientation oscillation is proportional to the total macroscopic deformation (Schwartz et al., 1999).

Transmission electron microscopy of grain interiors of both polycrystals and single crystals in orientations exhibiting multi-slip activity has shown that dislocations form cellular patterns with a stable wavelength inversely proportional to the accumulated plastic deformation. High-density bundles of dislocations form the cell walls, while the cell interiors remain mostly dislocation-free (Godfrey and Hughes, 2000). The majority of the dislocation content in cell walls is statistical in nature, meaning that it does not lead to any local lattice rotation; however, a small fraction ($\approx 1\%$) of the dislocation content in the walls is geometric in nature, leading to small lattice rotations of the type measured by Schwartz et al. (1999)

The length-scale dependence observed in crystal plasticity has been associated with the level of inhomogeneity in the plastic deformation. The classic examples of the Hall–Petch effect in polycrystals and the dislocation patterning in grain interiors have been established for decades. More recently, experiments have been conducted to further illuminate this length-scale dependence. Micro-indentation experiments of both single crystals and polycrystals have shown that the hardness decreases as the depth of indentation increases (Stelmashenko et al., 1993; Ma and Clarke, 1995; Nix and Gao, 1998). Experiments on the torsion of thin wires and on the bending of thin beams have shown similar behavior in which the torsional and bending flow strengths increased as specimen dimensions decreased (Fleck et al., 1994; Stölken and Evans, 1998).

Modeling such length-scale-dependent material behavior is not possible within the framework of classical continuum crystal plasticity (Follansbee and Kocks, 1988; Bronkhorst et al., 1992; Marin and Dawson, 1998; Nemat-Nasser et al., 1998). This class of constitutive models contains no intrinsic (material) length scale within its formulation. Since the increase in strength with decreasing scale can be related to proportional increases in the gradients of the overall strain field in each of the experiments, a class of models has been developed that incorporate a length scale dependence in the constitutive response of the material through functional dependencies on the plastic strain gradient (Mülhaus and Aifantis, 1991; Fleck and Hutchinson, 1997; Shu and Fleck, 1999; Gao et al., 1999; Acharya and Bassani, 2000). The physical basis for these models has been founded in dislocation mechanics; specifically, on theoretical developments concerning geometrically necessary dislocations (GNDs).

One can consider partitioning a density of crystallographic dislocations into a set having a net geometric consequence, and a complementary one lacking geometric consequence. Following Ashby (1970), the former have been labeled geometrically necessary dislocations and are related to the curvature of the crystal lattice and to the incompatibility of the plastic strain field (Nye, 1953; Bilby et al., 1955; Kröner, 1962; Cermelli and Gurtin, 2001), while the latter have been labeled statistically stored dislocations (SSDs) and are believed to result from random trapping processes that occur during "homogeneous" deformation of crystals. Therefore, a portion of the dislocation density in a crystal may be related to the plastic strain gradient field of a crystal.

At the differential volume element level, all dislocations are "geometrically necessary". Dislocation Dynamics (DD) simulation techniques have been developed that describe the plastic deformation of crystals at this level by tracking the motion and interaction of discrete dislocation line segments through the crystal (Kubin et al., 1992; Schwarz, 1999; Zbib et al., 1998). At the much larger volume element level typically used in continuum calculations of polycrystals, the dislocation density within the element is primarily composed of SSD density, and the GND density is ignored. However, for volume elements between these two extremes, particularly at the subgranular level, GND density cannot, in general, be ignored, yet the total dislocation content is too high for dislocations to be treated discretely. A continuum formulation incorporating the effects of SSD and GND densities should be considered to accurately describe the plasticity of crystals at this intermediate length scale.

In principle, the evolution of GND density is tractable because it is described by kinematic relationships related to the divergence of dislocation density flux. The level of detail with which the GND state is characterized in the aforementioned length-scale dependent models ranges from a strict interpretation of the dislocation tensor resolved crystallographically (Acharya and Bassani, 2000) to a loose interpretation of the GND state as a scalar invariant of all of the plastic strain gradients (Fleck and Hutchinson, 1997; Shu and Fleck, 1999), including gradient components not directly associated with the Nye dislocation tensor (Nye, 1953). Treatments of the evolution of the SSD population have been phenomenological in nature in all of the aforementioned models. Statistical dislocation densities have not been treated explicitly; instead, their effects on mechanical behavior have been described by strength evolution equations. The co-evolution of the SSD and GND densities must be prescribed, and an interaction between the two densities must be assumed a priori because they are quantitatively measured using different metrics.

Dislocation density-based state variable models have been developed for continuum crystal plasticity (Walgraef and Aifantis, 1985a, b; Cuitiño and Ortiz, 1992; Stainier et al., 2002), and have been successfully used to describe the large (length) scale deformation behavior of various metallic single crystals. The dislocation density state variables in these models represent SSD densities with limited geometric information. These densities are characterized by their Burgers vector, but their line senses, while being restricted, are undefined. To complement the evolution of the GND density, which is defined by both its Burgers vector and line sense, the evolution equations for SSD density must be extended to include information about their line sense, allowing them to be combined with the GND evolution equations to form general dislocation density evolution equations applicable over a range of length scales.

In this article, we develop a set of evolution equations for crystallographic dislocation densities that incorporates both polar (GND) and dipolar (SSD) dislocation densities. The evolution equations are based on basic principles in dislocation mechanics, generalized for a density basis. The polar portion of the evolution equations includes the accumulation or loss of geometric dislocation density due to both a non-zero divergence of dislocation flux and to geometric reactions that are accurate to the discrete dislocation level. The dipolar portion of the evolution equations includes the generation of dislocation density, based on the principle of dislocation line continuity, and the annihilation of dislocation density, based on the frequency of dipole encounters.

The dislocation evolution equations couple to the field equations and traction/displacement boundary conditions of traditional elastic–plastic initial boundary value problems, and introduce novel dislocation density/density-flux boundary conditions. A finite element implementation of the coupled system will be described and used to conduct a series of simple simulations. The simulations will be used to demonstrate the behavior of the model in incorporating material length scale-dependent behavior, and a discussion will follow on the physical nature of grain boundaries in light of the behavior of proposed model.

2. Continuum model description

We are interested in solving the mechanical equilibrium boundary value problem in a volume containing a single crystal with a network of dislocations, and the surface of the volume being subject to externally imposed tractions and displacements. The question arises: Is the boundary value problem well-posed? In general, the problem is not well-posed because there are additional degrees of freedom associated with motion of the dislocations that need to be specified; however, for large crystal volumes in which all of the dislocation density may be considered statistical in nature (i.e., having no geometric consequence), then the above boundary value problem is a valid approximation of the system.

In the following sections, a micro-mechanical theory of single-crystal plasticity will be developed that demonstrates the necessity of generalizing the above boundary value problem to accurately describe the nature of plastic deformation of crystals at micron length scales. The validity of the approximation for large crystal volumes will become evident in a selected illustrative example demonstrating essential features of the theory.

2.1. Crystal kinematics

The kinematics of the crystal plasticity formulation described below is based on the developments of Asaro and Rice (1977). The deformation gradient, $\mathbf{F} = \partial\mathbf{x}/\partial\mathbf{X}$, mapping a reference configuration of the material to the deformed configuration, is multiplicatively decomposed into elastic ($\mathbf{F}^{\mathrm{e}}$) and plastic ($\mathbf{F}^{\mathrm{p}}$) factors, such that

$$\mathbf{F} = \mathbf{F}^{\mathrm{e}}\mathbf{F}^{\mathrm{p}}, \tag{1}$$

where $\mathbf{F}^{\mathrm{p}}$, describing the effects of plastic deformation on an unrotated and undeformed crystal lattice, maps neighborhoods of the original configuration to intermediate ‘relaxed’ neighborhoods, and $\mathbf{F}^{\mathrm{e}}$ maps these intermediate neighborhoods to neighborhoods in the deformed configuration. Typically, $\mathbf{F}^{\mathrm{e}}$ involves small elastic stretches and arbitrary rigid-body rotations. With plastic deformation, $\mathbf{F}^{\mathrm{p}}$ evolves according to the flow rule

$$\dot{\mathbf{F}}^{\mathrm{p}} = \mathbf{L}^{\mathrm{p}}\mathbf{F}^{\mathrm{p}}, \tag{2}$$

where $\mathbf{L}^{\mathrm{p}}$ is the plastic flow rate. In crystals, $\mathbf{L}^{\mathrm{p}}$ is comprised of the superposition of the resolved crystallographic plastic shear rates, $\dot{\gamma}^{\alpha}$, such that

$$\mathbf{L}^{\mathrm{p}} = \sum_{\alpha} \dot{\gamma}^{\alpha}\mathbf{m}_0^{\alpha} \otimes \mathbf{n}_0^{\alpha}, \tag{3}$$

where $\mathbf{m}_0^{\alpha}$ and $\mathbf{n}_0^{\alpha}$ are unit lattice vectors in the reference configuration corresponding to the slip direction and the slip plane normal direction, respectively, for a given slip-system α.

An elastic strain measure, $\mathbf{E}^{\mathrm{e}}$, corresponding to the Cauchy–Green strain with respect to the intermediate configuration, is defined as

$$\mathbf{E}^{\mathrm{e}} \equiv \tfrac{1}{2}\{\mathbf{F}^{\mathrm{eT}}\mathbf{F}^{\mathrm{e}} - \mathbf{I}_2\}, \tag{4}$$

where $\mathbf{I}_2$ is the second-order identity tensor. The work-conjugate stress measure, $\bar{\mathbf{T}}$, is related to the Cauchy stress, $\mathbf{T}$, through the transformation $\bar{\mathbf{T}} = \det(\mathbf{F}^{\mathrm{e}})\mathbf{F}^{\mathrm{e}-1}\mathbf{T}\mathbf{F}^{\mathrm{e}-\mathrm{T}}$. Stress is related to elastic strain by

$$\bar{\mathbf{T}} = \mathscr{L}[\mathbf{E}^{\mathrm{e}}], \tag{5}$$

where $\mathscr{L}$ is the fourth-order tensor of crystallographic elastic moduli.

Connections between the single-crystal plasticity framework and the dislocation density state are made by (i) relating the motion and interaction of the crystallographic densities to the plastic shear rates in Eq. (3), and by (ii) quantifying the effects of the stress on the motion of the dislocation densities, and thus their evolution.

2.2. Crystallographic dislocation density basis

Crystallographic dislocation densities are defined by their magnitude, ρ, measured in line length per unit volume, Burgers vector, $\mathbf{b}$, and tangent line direction, $\mathbf{t}$. The Burgers vector space that a dislocation density may occupy is finite; however, the tangent line space is infinite, in general. To make the problem more computationally tractable, a dislocation density basis having a finite set of tangent line directions will be chosen to represent the general dislocation density state of the crystal. The choice of the dislocation density basis is in no way unique, but it should reflect the prevalence and importance of certain dislocation geometries in the real crystal yet be limited enough to make computations tractable.

The dislocation density basis used in this work will be: $\rho^{\alpha}_{\mathrm{e}+}$, $\rho^{\alpha}_{\mathrm{e}-}$, $\rho^{\alpha}_{\mathrm{s}+}$, $\rho^{\alpha}_{\mathrm{s}-}$, where subscripts e and s denote either pure edge or pure screw density, respectively; the sign of the subscript, $(+)$ or $(-)$, indicates the polarity of the dislocation density, and the superscript, α, denotes the slip-system. The superscripts and subscripts will also be used to associate various density-related quantities such as average dislocation segment lengths and velocities with each of the four dislocation densities comprising a given slip-system. This particular dislocation density basis was chosen here to include glissile dislocation densities and to keep the development of the evolution equations as simple as possible.

With the density basis chosen, the crystallographic plastic shear rates can be determined from the conservative glide of the densities on that slip-system by

$$\dot{\gamma}^{\alpha} = (\rho^{\alpha}_{\mathrm{e}+}\bar{v}^{\alpha}_{\mathrm{e}+} + \rho^{\alpha}_{\mathrm{e}-}\bar{v}^{\alpha}_{\mathrm{e}-} + \rho^{\alpha}_{\mathrm{s}+}\bar{v}^{\alpha}_{\mathrm{s}+} + \rho^{\alpha}_{\mathrm{s}-}\bar{v}^{\alpha}_{\mathrm{s}-})|\mathbf{b}^{\alpha}|, \tag{6}$$

where $\bar{v}$ is the average velocity of the associated density, and the product $\rho\bar{v}$ is the dislocation flux of the associated density. The sign convention on the sense of positive velocities is such that each (positive) dislocation flux increases the plastic shear rate of the slip-system.

Evolution equations must be developed for each of the dislocation densities included in the model, and constitutive functions for the average velocities for each of the densities must be specified. The evolution of the dislocation density in our sub-grain representative volume element is the cumulative result of three processes: generation, annihilation, and accumulation/loss associated with the dislocation flux divergence such that

$$\dot{\rho}^{\xi} = \dot{\rho}^{\xi}_{\mathrm{gen}} + \dot{\rho}^{\xi}_{\mathrm{ann}} + \dot{\rho}^{\xi}_{\mathrm{flux}} \tag{7}$$

for each dislocation density ξ in the model.[1] The generation and annihilation of dislocation density is statistical and does not change the overall geometric character of the dislocation density within the volume element. The flux divergence term leads to the evolution of GND density, and it is responsible for changes in the dislocation tensor of the volume element. Expressions for each of the three terms will be developed based on core concepts in dislocation mechanics.

2.3. Evolution of statistical dislocation density

The continuity of dislocation lines must be maintained as a crystal plastically deforms by the conservative glide of dislocations. Dislocation line segments must terminate

---

[1] Here, the superscript 'ξ' is shorthand indicating that Eq. (7) applies for each slip-system, and both dislocation characters and polarities.

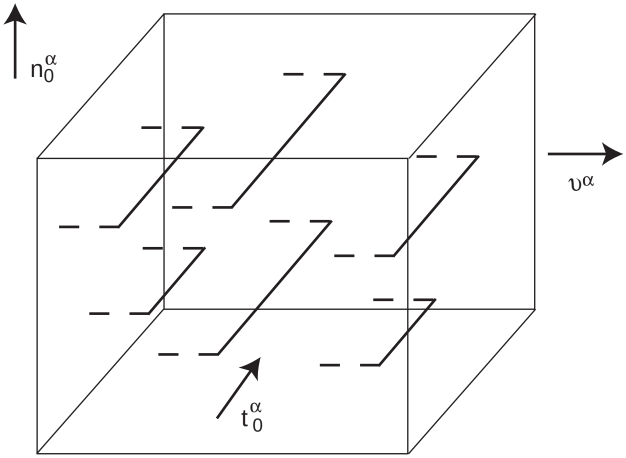

Fig. 1. Schematic depicting the generation of dislocation density by the motion of dislocation line segments as the crystal plastically deforms by dislocation glide.

only on other dislocation segments, free surfaces, grain boundaries, or other crystalline defects. As dislocation line segments glide, new dislocation line length must be generated to maintain the continuity of the lines. Consider Fig. 1 of a density of gliding dislocation segments. If the gliding segments represent edge dislocations, then dipole pairs of screw dislocations are left in their wake, connecting the segments back to the defect structures from which they originated. Likewise, gliding screw dislocation segments must leave pairs of edge dislocation dipoles in their wake. The length of the dislocation dipoles created is directly proportional to the distance traversed by the gliding segments and to the number density of the segments in the volume. In our discrete dislocation density basis, evolution equations of the form

$$\dot{\rho}^\alpha_{\mathrm{e+(gen)}} = \dot{\rho}^\alpha_{\mathrm{e-(gen)}} = \frac{\rho^\alpha_{\mathrm{s+}}|\bar{v}^\alpha_{\mathrm{s+}}|}{\bar{l}^\alpha_{\mathrm{s+}}} + \frac{\rho^\alpha_{\mathrm{s-}}|\bar{v}^\alpha_{\mathrm{s-}}|}{\bar{l}^\alpha_{\mathrm{s-}}}, \tag{8}$$

$$\dot{\rho}^\alpha_{\mathrm{s+(gen)}} = \dot{\rho}^\alpha_{\mathrm{s-(gen)}} = \frac{\rho^\alpha_{\mathrm{e+}}|\bar{v}^\alpha_{\mathrm{e+}}|}{\bar{l}^\alpha_{\mathrm{e+}}} + \frac{\rho^\alpha_{\mathrm{e-}}|\bar{v}^\alpha_{\mathrm{e-}}|}{\bar{l}^\alpha_{\mathrm{e-}}}, \tag{9}$$

where $\bar{l}$ is the average mobile segment length of the associated dislocation density, capture this growth mechanism of dislocation lines with plastic deformation. Within this context, the source of new density is the current density, and discrete dislocation configurations that lead to dislocation sources are assumed to exist within the volume element.

The key microstructural material parameter that quantifies the activity of dislocation sources and relates the amount of dislocation density generated per unit of shear is the average segment length. From detailed investigations of source activity in dislocation dynamics results (Arsenlis and Tang, 2003), the average segment lengths are observed to evolve during the course of plastic deformation. An evolution law for the average dislocation segment lengths of the form

$$\dot{\bar{l}}^{\alpha}_{e+} = \bar{l}^{\alpha}_{e+}\frac{\dot{\rho}^{\alpha}_{e+}}{\rho^{\alpha}_{e+}} - (\bar{l}^{\alpha}_{e+})^3[H^{\alpha\beta}_{ee}(\dot{\rho}^{\beta}_{e+} + \dot{\rho}^{\beta}_{e-}) + H^{\alpha\beta}_{es}(\dot{\rho}^{\beta}_{s+} + \dot{\rho}^{\beta}_{s-})], \tag{10}$$

$$\dot{\bar{l}}^{\alpha}_{e-} = \bar{l}^{\alpha}_{e-}\frac{\dot{\rho}^{\alpha}_{e-}}{\rho^{\alpha}_{e-}} - (\bar{l}^{\alpha}_{e-})^3[H^{\alpha\beta}_{ee}(\dot{\rho}^{\beta}_{e+} + \dot{\rho}^{\beta}_{e-}) + H^{\alpha\beta}_{es}(\dot{\rho}^{\beta}_{s+} + \dot{\rho}^{\beta}_{s-})], \tag{11}$$

$$\dot{\bar{l}}^{\alpha}_{s+} = \bar{l}^{\alpha}_{s+}\frac{\dot{\rho}^{\alpha}_{s+}}{\rho^{\alpha}_{s+}} - (\bar{l}^{\alpha}_{s+})^3[H^{\alpha\beta}_{se}(\dot{\rho}^{\beta}_{e+} + \dot{\rho}^{\beta}_{e-}) + H^{\alpha\beta}_{ss}(\dot{\rho}^{\beta}_{s+} + \dot{\rho}^{\beta}_{s-})], \tag{12}$$

$$\dot{\bar{l}}^{\alpha}_{s-} = \bar{l}^{\alpha}_{s-}\frac{\dot{\rho}^{\alpha}_{s-}}{\rho^{\alpha}_{s-}} - (\bar{l}^{\alpha}_{s-})^3[H^{\alpha\beta}_{se}(\dot{\rho}^{\beta}_{e+} + \dot{\rho}^{\beta}_{e-}) + H^{\alpha\beta}_{ss}(\dot{\rho}^{\beta}_{s+} + \dot{\rho}^{\beta}_{s-})], \tag{13}$$

where the $H^{\alpha\beta}$'s are segment-length interaction matrices, has been proposed based on observations of dislocation density growth in these detailed discrete dislocation simulations. The first terms on the right-hand sides of Eqs. (10)–(13) account for the lengthening of existing dislocation segments due to the aforementioned density growth mechanism, while the second term accounts for the introduction of nascent dislocation segments from dislocation sources within the crystal, acting to decrease the average segment length of the density within the volume. The first term keeps the number of dislocation segments in the volume, $\rho/\bar{l}$, constant, while the second term acts to increase the number of dislocation segments per unit volume due to multiplication processes.

The evolution equations for the statistical annihilation of dislocation density are based on dislocation interactions that act to reduce the total density of the system. All dislocation junction interactions can be considered as general dislocation annihilation reactions. Line lengths of the two junction-forming dislocations are eliminated, and a new junction dislocation is created, decreasing the internal energy of the dislocated crystal. The process can be considered statistical in two ways. There is a stochastic nature as to the frequency that such interactions occur in a plastically deforming crystal, and, in any event, the changes in the crystallographic dislocation densities do not affect the overall dislocation tensor of the volume because Burgers vectors are conserved at junction nodes.

The dislocation reaction most effective in reducing the total density of the system is the dipole-reaction, in which two equal-length dislocation line segments having the same tangent direction but opposite Burgers vectors react to eliminate their line lengths without creating a product junction dislocation. Consider Fig. 2 depicting a density of right-handed edge dislocations gliding past a density of left-handed edge dislocations moving in the opposite direction. Suppose that when two dislocations of opposite polarity come within a critical distance of one another, they mutually annihilate. If the dislocations are randomly distributed in the plane, the frequency with which a dislocation from the right-handed density comes within a critical distance of a dislocation of opposite polarity can be determined. A rate of dislocation density annihilation by this dipole-reaction may be approximated by

$$\dot{\rho}^{\alpha}_{e+(ann)} = \dot{\rho}^{\alpha}_{e-(ann)} = -\rho^{\alpha}_{e+}\rho^{\alpha}_{e-}R_e(|\bar{v}^{\alpha}_{e+}| + |\bar{v}^{\alpha}_{e-}|), \tag{14}$$

$$\dot{\rho}^{\alpha}_{s+(ann)} = \dot{\rho}^{\alpha}_{s-(ann)} = -\rho^{\alpha}_{s+}\rho^{\alpha}_{s-}R_s(|\bar{v}^{\alpha}_{s+}| + |\bar{v}^{\alpha}_{s-}|), \tag{15}$$

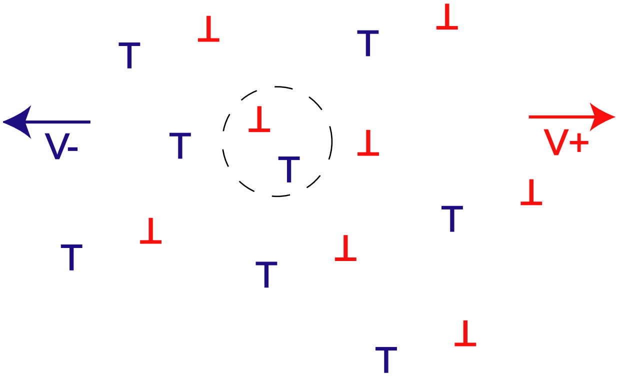

Fig. 2. Schematic depicting the reduction of dislocation density by the mutual annihilation of dislocation dipoles as the crystal plastically deforms by dislocation glide.

where R_e and R_s are the critical capture radii for the edge and screw dislocation densities, respectively. For simplicity, other dislocation reactions that can reduce the total dislocation density, albeit less effectively, will be ignored in this formulation. Neglect of other density-reducing mechanisms may lead to larger values of the critical capture radii within the simplified model than have been experimentally measured.

The generation and annihilation equations combine to describe the statistical evolution of dislocation density in a given volume. The generation terms dominate the evolution of the dislocation density at the low dislocation density levels typical of annealed crystals at low strains. The annihilation terms become proportionally larger as the dislocation density statistically accumulates, and they control the saturation level of the dislocation density. If there is a large disparity in the mobility of the edge and screw dislocation densities, as in BCC crystals, the less-mobile species will accumulate faster than the more mobile species (Arsenlis and Tang, 2003). If the flux-divergence part of the general dislocation density evolution is neglected, the two polar densities for each dislocation character may be consolidated into a single dipolar density without a loss of information, due to the symmetry in their evolution. The flux-divergence part of the dislocation density evolution equations, however, breaks that symmetry, so that densities of a given character, but of opposite sign, must be evolved separately.

2.4. Geometrically necessary dislocation density evolution

The evolution equations for the GND density are simpler to develop than those for the statistical density because they are closely connected to the inhomogeneous nature of plastic deformation in crystals. The GND density is related to the incompatibility of the plastic deformation and to the curvature of the underlying crystal lattice. In fact, it is that portion of the total density specifically needed to maintain the continuity of the crystal lattice.

The aggregate geometric properties of a dislocation density may be quantified by a dislocation density tensor, **A**, often termed Nye's tensor after Nye (1953). The tensor quantifies the net Burgers vector, $\mathbf{b}_{\text{net}}$, of a dislocation density piercing a unit surface area with normal, $\mathbf{n}_{\text{s}}$, through the expression

$$\mathbf{b}_{\text{net}} = \mathbf{A}\mathbf{n}_{\text{s}}. \tag{16}$$

The dislocation tensor of a volume can be determined by performing line integrals along all of the dislocation line segments contained in the volume (Arsenlis and Parks, 1999). In a discrete dislocation basis, the line integrals become tensorial sums of the densities in the basis given by

$$\mathbf{A} \equiv \sum_{\alpha} (\rho^{\alpha}_{\text{e}+} - \rho^{\alpha}_{\text{e}-})\mathbf{b}^{\alpha}_{0} \otimes \mathbf{p}^{\alpha}_{0} + (\rho^{\alpha}_{\text{s}+} - \rho^{\alpha}_{\text{s}-})\mathbf{b}^{\alpha}_{0} \otimes \mathbf{m}^{\alpha}_{0}, \tag{17}$$

where $\mathbf{p}^{\alpha}_{0} = \mathbf{m}^{\alpha}_{0} \times \mathbf{n}^{\alpha}_{0}$ is the tangent line direction of edge dislocation density on slip-system α. The dislocation tensor is a measure of the net polarity of the dislocation density contained in a volume element; therefore, dipole and other statistical densities do not contribute to the tensor.

Polarity develops in the dislocation density due to the inhomogeneous nature of plastic deformation and the discrete nature of dislocations. Dislocations originating from Frank–Read sources contained fully within a volume element add to the statistical density at their inception, but may later contribute to the polarity of the dislocation density elsewhere in the crystal. Polar dislocation density cannot be spontaneously created or annihilated in a volume, as can statistical dislocation density, because it would violate the conservation of Burgers vector law. Instead, polar dislocation density must be transported to/from some other region of the crystal, or result from local geometric reactions of existing polarity with dislocation flux.

Any discussion of the polarity in the dislocation density must also include a discussion of the volume over which that polarity is measured. If the representative volume element is smaller than the spacing between dislocations, every dislocation is polar and each is required to exist due to local lattice-geometric constraints. Dislocation dynamics simulations concern this length scale of simulation and trace the motion of individual dislocation lines through the crystal (Kubin et al., 1992; Zbib et al., 1998; Schwarz, 1999). Phase-field-based continuum models also treat this length scale of simulation (Ortiz, 1999; Wang et al., 2001) by restricting all of the dislocation density within their volume elements to be polar. Smaller representative volume elements have been treated with molecular dynamics and with preliminary work based on the theory of continuously distributed dislocations, in which a single dislocation may be represented by a distribution of density (Acharya, 2001) spanning multiple volume elements.

In our treatment, the representative volume element is assumed sufficiently large such that the polar/net-geometric part of the dislocation density is only a subset of the total density within the volume, necessitating the explicit consideration of dislocation dipoles and other statistical density. Furthermore, we assume that the defect structure can be represented adequately by a density of dislocations, and that each individual dislocation segment comprising the density need not be distinguished from the population. However, the evolution equations developed at this length scale for the polar dislocation density should remain valid when considering the behavior of a single dislocation, as in the treatment of Acharya (2001). At nanometer length scales, the evolution equations for the polarity in the dislocation density should be equivalent to rewriting the discrete dislocation dynamics formalism in a continuum control volume methodology.

Evolution of the dislocation tensor defined in Eq. (17) can be related to the plastic deformation history of the material. Kröner (1962) showed that certain gradients in the plastic deformation could be related to the dislocation tensor, leading Ashby (1970) to label this subset of the dislocation density as GND density. Within the finite deformation kinematics formalism using the multiplicative elastic–plastic decomposition of the total deformation gradient, several different expressions have been proposed for relating the dislocation tensor to referential derivatives of the plastic deformation or spatial derivatives of the inverse elastic deformation gradient. Dai and Parks (1997) have proposed $\mathbf{A}^{(\mathrm{DP})}=\mathrm{Curl}\ (\mathbf{F}^{\mathrm{p}})$. Acharya and Bassani (2000) have proposed $\mathbf{A}^{(\mathrm{AB})}=\mathrm{curl}\ (\mathbf{F}^{\mathrm{e}-1})$, while Cermelli and Gurtin (2001) have proposed $\mathbf{A}^{(\mathrm{CG})}=\mathrm{Curl}\ (\mathbf{F}^{\mathrm{p}})\ \mathbf{F}^{\mathrm{pT}}$, where the Curl of a tensor is defined via cartesian components as $C_{iq}=e_{qjk}\partial B_{ij}/\partial X_k$, and the curl of a tensor is defined as $C_{iq}=e_{qjk}\partial B_{ij}/\partial x_k$. Furthermore, Steinmann (1996) has shown that all of these measures of the dislocation tensor are related through appropriate configurational mappings. However, the question remains: which of these measures is most appropriately identified with the crystallographic dislocation density basis adopted in this formulation?

The plastic deformation in the multiplicative decomposition of the total deformation evolves in the intermediate configuration where $\mathbf{L}^{\mathrm{p}}$ is defined. In this configuration, the crystal is plastically deformed but elastically relaxed, and the lattice remains unrotated. Of the three measures mentioned above, only $\mathbf{A}^{(\mathrm{CG})}$ is defined in this material configuration. The time rate of change of $\mathbf{A}^{(\mathrm{CG})}$ can be decomposed into three parts, and each part may analyzed and directly related to geometric considerations found in simple discrete dislocation mechanics. The rate form of the adopted measure is

$$\dot{A}_{iq}^{(\mathrm{CG})}=e_{pjk}\frac{\partial L_{il}^{\mathrm{p}}}{\partial X_k}F_{lj}^{\mathrm{p}}F_{qp}^{\mathrm{p}}+L_{il}^{\mathrm{p}}A_{lq}^{(\mathrm{CG})}+A_{il}^{(\mathrm{CG})}L_{ql}^{\mathrm{p}}. \tag{18}$$

The first term on the right-hand side of Eq. (18) is related to the accumulation or loss of dislocation density of specific character and sign, due to divergence of that density's dislocation flux. The next two terms are geometric reactions that take place during plastic deformation by dislocation glide in a material element containing pre-existing polar dislocation content, and the physical significance of these reactions can be understood by investigating the underlying dislocation mechanisms they describe.

The tensors $\mathbf{L}^{\mathrm{p}}\mathbf{A}$ and $\mathbf{A}\mathbf{L}^{\mathrm{pT}}$ may be rewritten in terms of the dislocation density expressions in Eqs. (6) and (17), yielding

$$\mathbf{L}^{\mathrm{p}}\mathbf{A}=\sum_{\zeta}\sum_{\xi}\rho^{\zeta}\rho^{\xi}\bar{v}^{\zeta}(\mathbf{n}_0^{\zeta}\cdot\mathbf{b}_0^{\xi})\mathbf{b}_0^{\zeta}\otimes\mathbf{t}_0^{\xi}, \tag{19}$$

$$\mathbf{A}\mathbf{L}^{\mathrm{pT}}=\sum_{\zeta}\sum_{\xi}\rho^{\zeta}\rho^{\xi}\bar{v}^{\xi}(\mathbf{t}_0^{\zeta}\cdot\mathbf{n}_0^{\xi})\mathbf{b}_0^{\zeta}\otimes\mathbf{b}_0^{\xi}, \tag{20}$$

where $\mathbf{t}_0^{\zeta}$ is the tangent line direction of the dislocation density of index ζ, and ζ span the discrete space of crystallographic dislocation densities in the formulation. In our

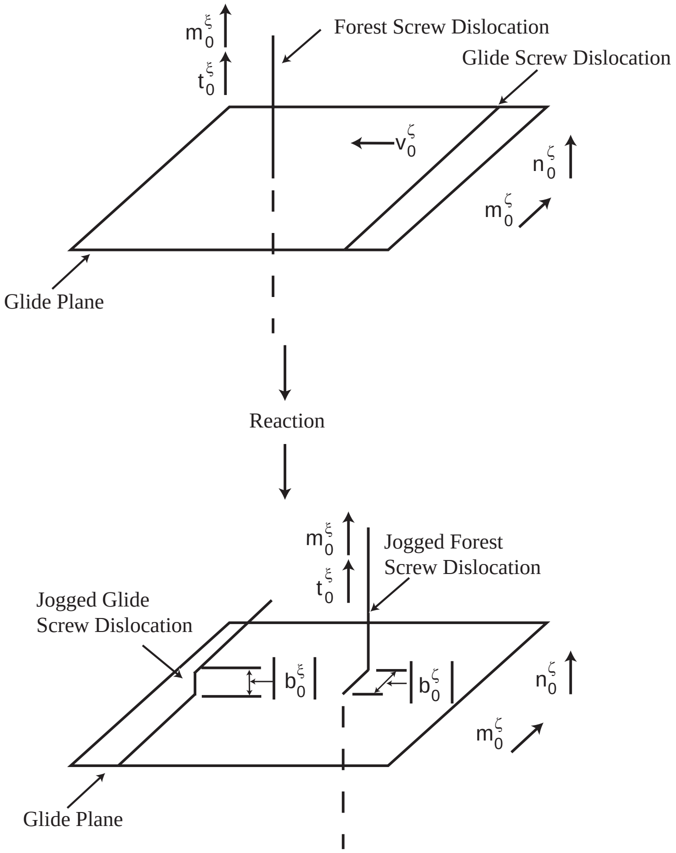

Fig. 3. Schematic depicting the forest reaction between two screw dislocations producing two jogged screw dislocations.

sign convention, $\mathbf{t}^\alpha_{0(\mathrm{e}+)} = -\mathbf{t}^\alpha_{0(\mathrm{e}-)} = \mathbf{p}^\alpha_0$, $\mathbf{t}^\alpha_{0(\mathrm{s}+)} = -\mathbf{t}^\alpha_{0(\mathrm{s}-)} = \mathbf{m}^\alpha_0$, and $\mathbf{b}^\alpha_{0(\mathrm{e}+)} = \mathbf{b}^\alpha_{0(\mathrm{e}-)} = \mathbf{b}^\alpha_{0(\mathrm{s}+)} = \mathbf{b}^\alpha_{0(\mathrm{s}-)} = |\mathbf{b}^\alpha_0|\mathbf{m}^\alpha_0$ for the four dislocation densities on every slip-system α. The dimensional similarity between Eqs. (19)–(20) and Eqs. (14)–(15) suggests that Eqs. (19)–(20) quantify the time rate of change in Nye's tensor due to geometric reactions, much as the annihilation rate equations quantify the reduction in the statistical density due to statistical reactions.

The geometric reactions can be further clarified through a series of three schematics, shown in Figs. 3–5, depicting the dislocation mechanisms captured by the two terms. The first mechanism, given in Fig. 3, depicts the geometric jog production associated with intersecting screw dislocation densities. The $\mathbf{A}\mathbf{L}^{\mathrm{p}^{\mathrm{T}}}$ term captures the rate of geometric jog/kink production in a geometric forest density due to gliding dislocation density. The $\mathbf{L}^{\mathrm{p}}\mathbf{A}$ term captures the rate of geometric jog production on the gliding dislocation density due to a forest of stationary geometrically necessary screw dislocations.

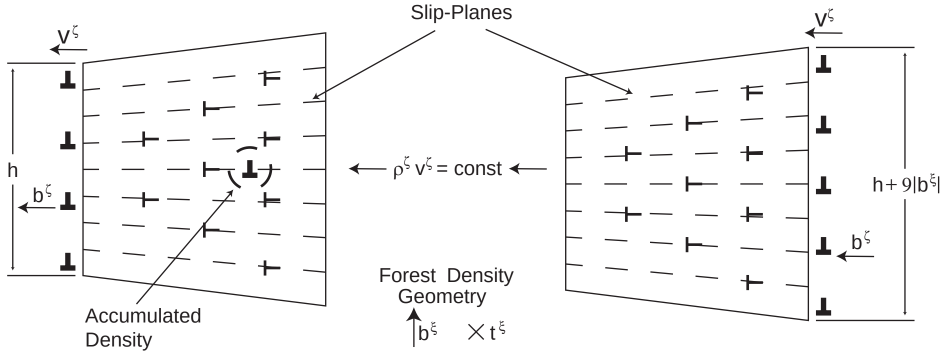

Fig. 4. Schematic depicting a constant flux of edge dislocation density gliding across converging planes through a geometrically dislocated crystal, leading to the accumulation of GND density in the volume. Given the amount of density accumulated in the volume, the height is equal to $h = 36|\mathbf{b}|$.

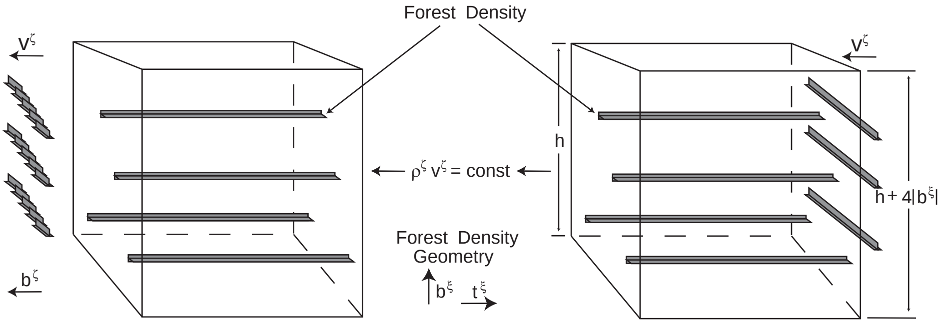

Fig. 5. Schematic depicting a constant flux of edge dislocation density gliding across converging planes through a geometrically dislocated crystal, leading to the development of screw kinks on the glide density.

The $\mathbf{L}^p\mathbf{A}$ term also captures the effect of converging/diverging slip planes which result from a local accumulation of dislocations of the same character. If the slip planes converge in the direction of motion of the density, as depicted in Fig. 4, an equal dislocation density flux across both of the faces leads to an accumulation of density within the volume, due to the difference in area of those faces. Similarly, homogeneous plastic deformation in volumes with slip planes converging in the tangent line direction of the gliding dislocations, as shown in Fig. 5, leads to the formation of kinks on the gliding dislocations due to the change in the cross-sectional area of the volume along the line of the dislocation. The $\mathbf{L}^p\mathbf{A}$ and $\mathbf{A}\mathbf{L}^{p^T}$ terms are physically justified as geometric reactions occurring in geometrically dislocated crystals.

The evolution rate for $\mathbf{A}$ described in terms of continuum variables above needs to be tied to dislocation density evolution rates. By taking the time derivative of Eq. (17)

and combining it with Eq. (18), the following equality may be formed:

$$\sum_{\alpha} b^{\alpha}_{0(i)}[(\dot{\rho}^{\alpha}_{\mathrm{e}+(\mathrm{flux})} - \dot{\rho}^{\alpha}_{\mathrm{e}-(\mathrm{flux})})p^{\alpha}_{0(q)} + (\dot{\rho}^{\alpha}_{\mathrm{s}+(\mathrm{flux})} - \dot{\rho}^{\alpha}_{\mathrm{s}-(\mathrm{flux})})m^{\alpha}_{0(q)}]$$

$$= e_{pjk}\frac{\partial L^{\mathrm{p}}_{il}}{\partial X_k} F^{\mathrm{p}}_{lj}F^{\mathrm{p}}_{qp} + L^{\mathrm{p}}_{il}A_{lq} + A_{il}L^{\mathrm{p}}_{ql}. \tag{21}$$

However, $\dot{\rho}^{\alpha}_{\mathrm{e}+(\mathrm{flux})}$, $\dot{\rho}^{\alpha}_{\mathrm{e}-(\mathrm{flux})}$, $\dot{\rho}^{\alpha}_{\mathrm{s}+(\mathrm{flux})}$, and $\dot{\rho}^{\alpha}_{\mathrm{s}-(\mathrm{flux})}$ cannot be uniquely determined from Eq. (21). While Eq. (21) constrains the evolution of the slip-system dislocation densities to maintain the continuity of the crystal lattice, it does not precisely specify the crystallographic dislocation configuration that develops. It is clearly evident from Eq. (21), for example, that accumulation of a certain amount of $\rho^{\alpha}_{\mathrm{e}+}$ would have the same geometric consequence as a loss of the same amount of $\rho^{\alpha}_{\mathrm{e}-}$, and the right-hand side of the equation neither requires nor favors one of these kinetic processes over the other.

By appealing to certain physical considerations, a reasonable set of evolution equations may be developed by assuming that the polarity of the dislocation density in a given slip-system results from processes involving dislocation densities within that slip-system. By rewriting $\mathbf{L}^{\mathrm{p}}$ in terms of the crystallographic dislocation fluxes that constitute it and separating the contributions of each of the dislocation densities within each slip-system to $\dot{\mathbf{A}}$, the flux divergence contribution to the crystallographic dislocation density evolution may take the form

$$\begin{aligned}\dot{\rho}^{\alpha}_{\mathrm{e}+(\mathrm{flux})} = &-\frac{\partial}{\partial \mathbf{X}}[\rho^{\alpha}_{\mathrm{e}+}\bar{v}^{\alpha}_{\mathrm{e}+} + f_{\mathrm{e}}(\rho^{\alpha}_{\mathrm{s}+}\bar{v}^{\alpha}_{\mathrm{s}+} + \rho^{\alpha}_{\mathrm{s}-}\bar{v}^{\alpha}_{\mathrm{s}-})]\cdot(\mathbf{F}^{\mathrm{p}^{-1}}\mathbf{m}^{\alpha}_0)\\ &+(\mathbf{n}^{\alpha}_0\cdot\mathbf{A}\mathbf{p}^{\alpha}_0)[\rho^{\alpha}_{\mathrm{e}+}\bar{v}^{\alpha}_{\mathrm{e}+} + f_{\mathrm{e}}(\rho^{\alpha}_{\mathrm{s}+}\bar{v}^{\alpha}_{\mathrm{s}+} + \rho^{\alpha}_{\mathrm{s}-}\bar{v}^{\alpha}_{\mathrm{s}-})]\\ &+\rho^{\alpha}_{\mathrm{e}+}\mathbf{p}^{\alpha}_0\cdot\mathbf{L}^{\mathrm{p}}\mathbf{p}^{\alpha}_0 + f_{\mathrm{e}}(\rho^{\alpha}_{\mathrm{s}+} - \rho^{\alpha}_{\mathrm{s}-})\mathbf{p}^{\alpha}_0\cdot\mathbf{L}^{\mathrm{p}}\mathbf{m}^{\alpha}_0,\end{aligned} \tag{22}$$

$$\begin{aligned}\dot{\rho}^{\alpha}_{\mathrm{e}-(\mathrm{flux})} = &\frac{\partial}{\partial \mathbf{X}}[\rho^{\alpha}_{\mathrm{e}-}\bar{v}^{\alpha}_{\mathrm{e}-} + (1-f_{\mathrm{e}})(\rho^{\alpha}_{\mathrm{s}+}\bar{v}^{\alpha}_{\mathrm{s}+} + \rho^{\alpha}_{\mathrm{s}-}\bar{v}^{\alpha}_{\mathrm{s}-})]\cdot(\mathbf{F}^{\mathrm{p}^{-1}}\mathbf{m}^{\alpha}_0)\\ &-(\mathbf{n}^{\alpha}_0\cdot\mathbf{A}\mathbf{p}^{\alpha}_0)[\rho^{\alpha}_{\mathrm{e}-}\bar{v}^{\alpha}_{\mathrm{e}-} + (1-f_{\mathrm{e}})(\rho^{\alpha}_{\mathrm{s}+}\bar{v}^{\alpha}_{\mathrm{s}+} + \rho^{\alpha}_{\mathrm{s}-}\bar{v}^{\alpha}_{\mathrm{s}-})]\\ &+\rho^{\alpha}_{\mathrm{e}-}\mathbf{p}^{\alpha}_0\cdot\mathbf{L}^{\mathrm{p}}\mathbf{p}^{\alpha}_0 - (1-f_{\mathrm{e}})(\rho^{\alpha}_{\mathrm{s}+} - \rho^{\alpha}_{\mathrm{s}-})\mathbf{p}^{\alpha}_0\cdot\mathbf{L}^{\mathrm{p}}\mathbf{m}^{\alpha}_0,\end{aligned} \tag{23}$$

$$\begin{aligned}\dot{\rho}^{\alpha}_{\mathrm{s}+(\mathrm{flux})} = &\frac{\partial}{\partial \mathbf{X}}[\rho^{\alpha}_{\mathrm{s}+}\bar{v}^{\alpha}_{\mathrm{s}+} + f_{\mathrm{s}}(\rho^{\alpha}_{\mathrm{e}+}\bar{v}^{\alpha}_{\mathrm{e}+} + \rho^{\alpha}_{\mathrm{e}-}\bar{v}^{\alpha}_{\mathrm{e}-})]\cdot(\mathbf{F}^{\mathrm{p}^{-1}}\mathbf{p}^{\alpha}_0)\\ &+(\mathbf{n}^{\alpha}_0\cdot\mathbf{A}\mathbf{m}^{\alpha}_0)[\rho^{\alpha}_{\mathrm{s}+}\bar{v}^{\alpha}_{\mathrm{s}+} + f_{\mathrm{s}}(\rho^{\alpha}_{\mathrm{e}+}\bar{v}^{\alpha}_{\mathrm{e}+} + \rho^{\alpha}_{\mathrm{e}-}\bar{v}^{\alpha}_{\mathrm{e}-})]\\ &+\rho^{\alpha}_{\mathrm{s}+}\mathbf{m}^{\alpha}_0\cdot\mathbf{L}^{\mathrm{p}}\mathbf{m}^{\alpha}_0 + f_{\mathrm{s}}(\rho^{\alpha}_{\mathrm{e}+} - \rho^{\alpha}_{\mathrm{e}-})\mathbf{m}^{\alpha}_0\cdot\mathbf{L}^{\mathrm{p}}\mathbf{p}^{\alpha}_0,\end{aligned} \tag{24}$$

$$\begin{aligned}\dot{\rho}^{\alpha}_{\mathrm{s}-(\mathrm{flux})} = &-\frac{\partial}{\partial \mathbf{X}}[\rho^{\alpha}_{\mathrm{s}-}\bar{v}^{\alpha}_{\mathrm{s}-} + (1-f_{\mathrm{s}})(\rho^{\alpha}_{\mathrm{e}+}\bar{v}^{\alpha}_{\mathrm{e}+} + \rho^{\alpha}_{\mathrm{e}-}\bar{v}^{\alpha}_{\mathrm{e}-})]\cdot(\mathbf{F}^{\mathrm{p}^{-1}}\mathbf{p}^{\alpha}_0)\\ &-(\mathbf{n}^{\alpha}_0\cdot\mathbf{A}\mathbf{m}^{\alpha}_0)[\rho^{\alpha}_{\mathrm{s}-}\bar{v}^{\alpha}_{\mathrm{s}-} + (1-f_{\mathrm{s}})(\rho^{\alpha}_{\mathrm{e}+}\bar{v}^{\alpha}_{\mathrm{e}+} + \rho^{\alpha}_{\mathrm{e}-}\bar{v}^{\alpha}_{\mathrm{e}-})]\\ &+\rho^{\alpha}_{\mathrm{s}-}\mathbf{m}^{\alpha}_0\cdot\mathbf{L}^{\mathrm{p}}\mathbf{m}^{\alpha}_0 - (1-f_{\mathrm{s}})(\rho^{\alpha}_{\mathrm{e}+} - \rho^{\alpha}_{\mathrm{e}-})\mathbf{m}^{\alpha}_0\cdot\mathbf{L}^{\mathrm{p}}\mathbf{p}^{\alpha}_0,\end{aligned} \tag{25}$$

$$\dot{\rho}^{\alpha}_{j\pm(\mathrm{flux})} = (\mathbf{n}^{\alpha}_0 \cdot \mathbf{A}\mathbf{n}^{\alpha}_0)[\rho^{\alpha}_{\mathrm{e}+}\bar{v}^{\alpha}_{\mathrm{e}+} + \rho^{\alpha}_{\mathrm{e}-}\bar{v}^{\alpha}_{\mathrm{e}-} + \rho^{\alpha}_{\mathrm{s}+}\bar{v}^{\alpha}_{\mathrm{s}+} + \rho^{\alpha}_{\mathrm{s}-}\bar{v}^{\alpha}_{\mathrm{s}-}]$$
$$+ (\rho^{\alpha}_{\mathrm{e}+} - \rho^{\alpha}_{\mathrm{e}-})\mathbf{n}^{\alpha}_0 \cdot \mathbf{L}^{\mathrm{p}}\mathbf{p}^{\alpha}_0 + (\rho^{\alpha}_{\mathrm{s}+} - \rho^{\alpha}_{\mathrm{s}-})\mathbf{n}^{\alpha}_0 \cdot \mathbf{L}^{\mathrm{p}}\mathbf{m}^{\alpha}_0, \tag{26}$$

where $\dot{\rho}^{\alpha}_{j\pm}$ is the rate of production of geometrically necessary jog density, and f_{e} and f_{s} are dimensionless functions with the following properties:

$$0 \leqslant f_{\mathrm{e}}[\rho^{\alpha}_{\mathrm{e}+}, \rho^{\alpha}_{\mathrm{e}-}] \leqslant 1, \quad f_{\mathrm{e}}[\rho^{\alpha}_{\mathrm{e}+} = 0, \rho^{\alpha}_{\mathrm{e}-}] = 0,$$

$$f_{\mathrm{e}}[\rho^{\alpha}_{\mathrm{e}+}, \rho^{\alpha}_{\mathrm{e}-} = 0] = 1, \quad f_{\mathrm{e}}[\rho^{\alpha}_{\mathrm{e}+} = \rho^{\alpha}_{\mathrm{e}-}, \rho^{\alpha}_{\mathrm{e}-}] = \tfrac{1}{2},$$

$$0 \leqslant f_{\mathrm{s}}[\rho^{\alpha}_{\mathrm{s}+}, \rho^{\alpha}_{\mathrm{s}-}] \leqslant 1, \quad f_{\mathrm{s}}[\rho^{\alpha}_{\mathrm{s}+} = 0, \rho^{\alpha}_{\mathrm{s}-}] = 0,$$

$$f_{\mathrm{s}}[\rho^{\alpha}_{\mathrm{s}+}, \rho^{\alpha}_{\mathrm{s}-} = 0] = 1, \quad f_{\mathrm{s}}[\rho^{\alpha}_{\mathrm{s}+} = \rho^{\alpha}_{\mathrm{s}-}, \rho^{\alpha}_{\mathrm{s}-}] = \tfrac{1}{2}.$$

The functions f_{e} and f_{s} are used to ensure that all of the crystallographic dislocation densities remain non-negative during the deformation.

The different components of each of the resulting expressions can be analyzed separately to understand their respective physical significances. Focusing on Eq. (22), the first term in the expression is a measure of the divergence of the dislocation density flux. The functional dependence of **A** on Curl $\mathbf{F}^{\mathrm{p}}$ translates into a relationship between $\dot{\rho}^{\xi}_{(\mathrm{flux})}$ and Div $[\rho^{\xi}\bar{v}^{\xi}]$. Within the brackets of the first line, the first term quantifies the difference in the right-handed dislocation density entering and exiting the volume element, and the second term quantifies the production/removal of edge kink density resulting from differences in the velocity of the screw density along their line lengths. The f_{e} function is used to apportion the kink accumulation/loss rate between the right- and left-handed edge densities. The assumption that the kink density always increases is only valid if the screw dislocations moving through the crystal are kink-free as they enter the volume.

The next two lines of Eq. (22) quantify the geometric reactions already discussed in detail in conjunction with Figs. 3–5. The second line of Eq. (22) derives from the $\mathbf{L}^{\mathrm{p}}\mathbf{A}$ term in Eq. (18). The third line of Eq. (22) derives from the $\mathbf{A}\mathbf{L}^{\mathrm{p}\mathrm{T}}$ term in Eq. (18). The corresponding expressions for $\dot{\rho}^{\alpha}_{\mathrm{e}-}$, $\dot{\rho}^{\alpha}_{\mathrm{s}+}$, and $\dot{\rho}^{\alpha}_{\mathrm{s}-}$ in Eqs. (23)–(25) all follow from similar physical considerations.

A jog density has not been explicitly incorporated into the model to this point, mainly because climb of edge dislocations has been ignored, and the density of jogs formed by statistical interactions of gliding densities is assumed to be much lower than the edge and screw densities in the slip-system. However, if the jog density evolution rate is ignored, the equality in Eq. (21) no longer holds. The crystallographic dislocation density space we have employed does not need to be increased in dimension to account for the geometric jog density in highly symmetric crystals. The jog density on one slip-system could be alternatively represented by a combination of edge density on that slip-system and edge density on a cross-slip plane. Fig. 6 shows the geometric equivalence of a dislocation jog to a combination of edge dislocations on cross-slip planes. This representation of jog density in highly symmetric crystals maintains the dimensionality of the crystallographic dislocation density basis while capturing the geometric evolution of dislocation jogs in the crystal.

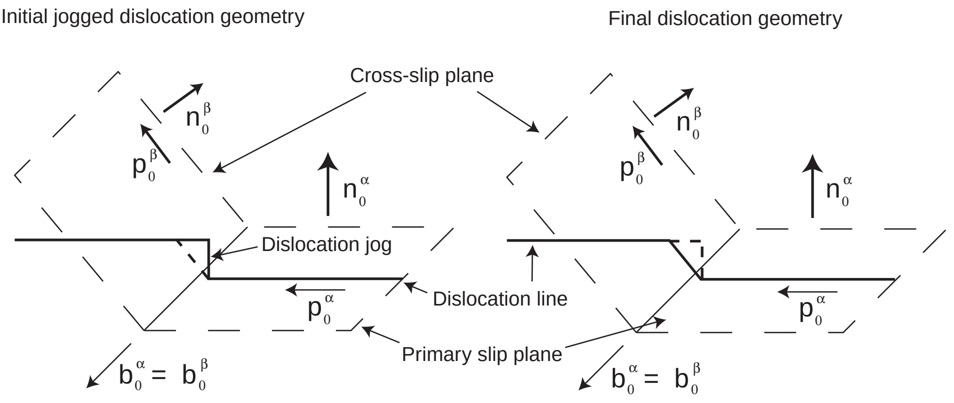

Fig. 6. Reconstruction of a dislocation jog by appropriate lengths of edge dislocations on a pair of slip-systems sharing a common Burgers vector.

The contribution of the dislocation flux divergence to the dislocation density evolution breaks the symmetry between the polar edge and screw densities, but it's ambiguous whether the total dislocation density increases as a result. Existing "strain-gradient plasticity" models used to simulate the material length scale-dependent nature of crystal plasticity either explicitly or implicitly assume that the geometric density augments the total dislocation density when compared to the dislocation density evolution in a "homogeneously" deforming crystal. From the evolution Eqs. (22)–(26), the geometric portion of the dislocation density evolution does not necessarily increase the total dislocation density. It may also decrease the total density. Whether dislocation density is accumulated or lost due to the flux divergence depends on the participation of the relative densities to the plastic deformation across the volume and on the sign of their divergence. If positive edge dislocations are the only species within a volume, and the plastic deformation field is such that more edge dislocations leave the volume than enter the volume, the total density in the volume will decrease as a result of the inhomogeneous plastic deformation. The assumption that GND density "adds" to a background SSD density is, in general, not justified when viewed from this dislocation basis.

2.5. Constitutive equations

Along with the constitutive equation relating the stress to the elastic strain in Eq. (5), the dislocation density evolution equations included several quantities that need to be constitutively defined to complete the model. The average dislocation velocity, the average segment length interaction matrices, and the critical capture radii all need to be specified. The average dislocation velocity function is most directly related to the evolution of the stress–strain response of the crystal, while the average segment length matrices and the critical capture radii determine the statistical evolution of the dislocation density.

The dependence of these three quantities may, in general, depend on

$$\bar{v}^{\zeta} = \hat{\bar{v}}^{\zeta}[\bar{\mathbf{T}}, \theta, \rho^{\xi}, \mathbf{F}^{\mathrm{p-T}}\,\mathrm{Grad}\,\rho^{\xi}, \mathbf{m}_0^{\xi}, \mathbf{n}_0^{\xi}, \mathbf{t}_0^{\xi}], \tag{27}$$

$$R^{\zeta} = \hat{R}^{\zeta}[\bar{\mathbf{T}}, \theta, \rho^{\xi}, \mathbf{F}^{\mathrm{p-T}}\,\mathrm{Grad}\,\rho^{\xi}, \mathbf{m}_0^{\xi}, \mathbf{n}_0^{\xi}, \mathbf{t}_0^{\xi}], \tag{28}$$

$$H^{\zeta\xi} = \hat{H}^{\zeta\xi}[\bar{\mathbf{T}}, \theta, \rho^{\xi}, \mathbf{F}^{\mathrm{p-T}}\,\mathrm{Grad}\,\rho^{\xi}, \mathbf{m}_0^{\xi}, \mathbf{n}_0^{\xi}, \mathbf{t}_0^{\xi}], \tag{29}$$

the second Piola–Kirchhoff stress in the intermediate configuration, $\bar{\mathbf{T}}$; temperature, θ; dislocation density state, ρ^{ξ}; gradients of the dislocation density in the intermediate configuration, $\mathbf{F}^{\mathrm{p-T}}\,\mathrm{Grad}\,\rho^{\xi}$; and the crystal geometry: $\mathbf{m}_0^{\xi}, \mathbf{n}_0^{\xi}, \mathbf{t}_0^{\xi}$. The functional dependencies on the stress, temperature, dislocation (material) state, and geometry are commonplace; however, the dependence of constitutive functions on gradients of the dislocation density state is not as common and deserves further attention.

Constitutive models have been developed in which the evolution of dislocation density depends on gradients of the density (Walgraef and Aifantis, 1988; Sluys and Estrin, 2000). The gradients of the density have been used to introduce diffusion-like terms into the dislocation density evolution, whereby the flux of dislocation density is proportional to the gradients of the density; however, the evolution of the polarity of the density is not expressly considered. Dislocation gradient-dependent constitutive functions have also been proposed within the geometrically necessary dislocation density framework (Menzel and Steinmann, 2000; Gurtin, 2002). The dislocation gradient-dependent “configurational stresses” in these models arise from proposed free energy dependencies on the density tensor. Here a stress, dependent in part on the gradients of the polarity, will be included in the constitutive equations for the average dislocation velocity in order to incorporate scale-dependent stress–strain response in the model.

3. Finite element implementation and boundary conditions

The finite element implementation of equilibrium field equations is common; therefore, it will not be discussed here. However, the dislocation density evolution equations developed in the previous section involve referential gradients of the dislocation flux, and calculating the dislocation density evolution in a finite element framework is non-trivial. Furthermore, the dependence of certain constitutive functions on gradients of the dislocation density means that each of the dislocation densities must be treated as temporally evolving and spatially varying field variables. As (nodal) degrees of freedom within the finite element interpolation framework, the dislocation densities and their gradients would be available to calculate the constitutive response of the material at the quadrature points within the element.

The discussion here will focus on the implementation of the evolution equation for $\rho_{\mathrm{e}+}^{\alpha}$. The evolution equations for the other crystallographic dislocation densities in the model are similar in nature and would make the discussion redundant. The total evolution equation for $\rho_{\mathrm{e}+}^{\alpha}$ from the three different components in the previous section is

$$\begin{aligned}0 = {} & \dot{\rho}^{\alpha}_{\mathrm{e}+} - \frac{\rho^{\alpha}_{\mathrm{s}+}|\bar{v}^{\alpha}_{\mathrm{s}+}|}{\bar{l}^{\alpha}_{\mathrm{s}+}} - \frac{\rho^{\alpha}_{\mathrm{s}-}|\bar{v}^{\alpha}_{\mathrm{s}-}|}{\bar{l}^{\alpha}_{\mathrm{s}-}} + \rho^{\alpha}_{\mathrm{e}+}\rho^{\alpha}_{\mathrm{e}-}R_{\mathrm{e}}(|\bar{v}^{\alpha}_{\mathrm{e}+}| + |\bar{v}^{\alpha}_{\mathrm{e}-}|) \\ & + \frac{\partial}{\partial \mathbf{X}}[\rho^{\alpha}_{\mathrm{e}+}\bar{v}^{\alpha}_{\mathrm{e}+} + f_{\mathrm{e}}(\rho^{\alpha}_{\mathrm{s}+}\bar{v}^{\alpha}_{\mathrm{s}+} + \rho^{\alpha}_{\mathrm{s}-}\bar{v}^{\alpha}_{\mathrm{s}-})] \cdot (\mathbf{F}^{\mathrm{p}-1}\mathbf{m}^{\alpha}_{0}) \\ & - (\mathbf{n}^{\alpha}_{0} \cdot \mathbf{A}\mathbf{p}^{\alpha}_{0})[\rho^{\alpha}_{\mathrm{e}+}\bar{v}^{\alpha}_{\mathrm{e}+} + f_{\mathrm{e}}(\rho^{\alpha}_{\mathrm{s}+}\bar{v}^{\alpha}_{\mathrm{s}+} + \rho^{\alpha}_{\mathrm{s}-}\bar{v}^{\alpha}_{\mathrm{s}-})] \\ & - \rho^{\alpha}_{\mathrm{e}+}\mathbf{p}^{\alpha}_{0} \cdot \mathbf{L}^{\mathrm{p}}\mathbf{p}^{\alpha}_{0} - f_{\mathrm{e}}(\rho^{\alpha}_{\mathrm{s}+} - \rho^{\alpha}_{\mathrm{s}-})\mathbf{p}^{\alpha}_{0} \cdot \mathbf{L}^{\mathrm{p}}\mathbf{m}^{\alpha}_{0}. \end{aligned} \tag{30}$$

The evolution equation may be multiplied by a virtual density, $\tilde{\rho}$, and integrated over a volume, V, in the reference configuration leading to

$$\begin{aligned}0 = {} & \int_V \tilde{\rho}\dot{\rho}^{\alpha}_{\mathrm{e}+}\,\mathrm{d}V - \int_V \tilde{\rho}\,\frac{\rho^{\alpha}_{\mathrm{s}+}|\bar{v}^{\alpha}_{\mathrm{s}+}|}{\bar{l}^{\alpha}_{\mathrm{s}+}}\,\mathrm{d}V - \int_V \tilde{\rho}\,\frac{\rho^{\alpha}_{\mathrm{s}-}|\bar{v}^{\alpha}_{\mathrm{s}-}|}{\bar{l}^{\alpha}_{\mathrm{s}-}}\,\mathrm{d}V \\ & + \int_V \tilde{\rho}\rho^{\alpha}_{\mathrm{e}+}\rho^{\alpha}_{\mathrm{e}-}R_{\mathrm{e}}(|\bar{v}^{\alpha}_{\mathrm{e}+}| + |\bar{v}^{\alpha}_{\mathrm{e}-}|)\,\mathrm{d}V \\ & + \int_V \tilde{\rho}\,\frac{\partial}{\partial \mathbf{X}}\,[\rho^{\alpha}_{\mathrm{e}+}\bar{v}^{\alpha}_{\mathrm{e}+} + f_{\mathrm{e}}(\rho^{\alpha}_{\mathrm{s}+}\bar{v}^{\alpha}_{\mathrm{s}+} + \rho^{\alpha}_{\mathrm{s}-}\bar{v}^{\alpha}_{\mathrm{s}-})] \cdot (\mathbf{F}^{\mathrm{p}-1}\mathbf{m}^{\alpha}_{0})\,\mathrm{d}V \\ & - \int_V \tilde{\rho}(\mathbf{n}^{\alpha}_{0} \cdot \mathbf{A}\mathbf{p}^{\alpha}_{0})[\rho^{\alpha}_{\mathrm{e}+}\bar{v}^{\alpha}_{\mathrm{e}+} + f_{\mathrm{e}}(\rho^{\alpha}_{\mathrm{s}+}\bar{v}^{\alpha}_{\mathrm{s}+} + \rho^{\alpha}_{\mathrm{s}-}\bar{v}^{\alpha}_{\mathrm{s}-})]\,\mathrm{d}V \\ & - \int_V \tilde{\rho}\rho^{\alpha}_{\mathrm{e}+}\mathbf{p}^{\alpha}_{0} \cdot \mathbf{L}^{\mathrm{p}}\mathbf{p}^{\alpha}_{0}\,\mathrm{d}V - \int_V \tilde{\rho}f_{\mathrm{e}}(\rho^{\alpha}_{\mathrm{s}+} - \rho^{\alpha}_{\mathrm{s}-})\mathbf{p}^{\alpha}_{0} \cdot \mathbf{L}^{\mathrm{p}}\mathbf{m}^{\alpha}_{0}\,\mathrm{d}V. \end{aligned} \tag{31}$$

Eq. (31) cannot be implemented within an FEM framework as it stands because the average dislocation velocities must be specified in the constitutive functions, and are not nodal quantities that can be readily interpolated. By using the Divergence Theorem and integrating by parts, the referential space derivatives may removed from the dislocation density fluxes and placed on the virtual density. The final weak form of Eq. (31) becomes

$$\begin{aligned}0 = {} & \int_V \tilde{\rho}\dot{\rho}^{\alpha}_{\mathrm{e}+}\,\mathrm{d}V - \int_V \tilde{\rho}\,\frac{\rho^{\alpha}_{\mathrm{s}+}|\bar{v}^{\alpha}_{\mathrm{s}+}|}{\bar{l}^{\alpha}_{\mathrm{s}+}}\,\mathrm{d}V - \int_V \tilde{\rho}\,\frac{\rho^{\alpha}_{\mathrm{s}-}|\bar{v}^{\alpha}_{\mathrm{s}-}|}{\bar{l}^{\alpha}_{\mathrm{s}-}}\,\mathrm{d}V \\ & + \int_V \tilde{\rho}\rho^{\alpha}_{\mathrm{e}+}\rho^{\alpha}_{\mathrm{e}-}R_{\mathrm{e}}(|\bar{v}^{\alpha}_{\mathrm{e}+}| + |\bar{v}^{\alpha}_{\mathrm{e}-}|)\,\mathrm{d}V \\ & - \int_V \frac{\partial \tilde{\rho}}{\partial \mathbf{X}} \cdot (\mathbf{F}^{\mathrm{p}-1}\mathbf{m}^{\alpha}_{0})[\rho^{\alpha}_{\mathrm{e}+}\bar{v}^{\alpha}_{\mathrm{e}+} + f_{\mathrm{e}}(\rho^{\alpha}_{\mathrm{s}+}\bar{v}^{\alpha}_{\mathrm{s}+} + \rho^{\alpha}_{\mathrm{s}-}\bar{v}^{\alpha}_{\mathrm{s}-})]\,\mathrm{d}V \\ & - \int_V \tilde{\rho}(\mathbf{p}^{\alpha}_{0} \cdot \mathbf{A}\mathbf{n}^{\alpha}_{0})[\rho^{\alpha}_{\mathrm{e}+}\bar{v}^{\alpha}_{\mathrm{e}+} + f_{\mathrm{e}}(\rho^{\alpha}_{\mathrm{s}+}\bar{v}^{\alpha}_{\mathrm{s}+} + \rho^{\alpha}_{\mathrm{s}-}\bar{v}^{\alpha}_{\mathrm{s}-})]\,\mathrm{d}V \end{aligned}$$

$$
\begin{aligned}
&-\int_V \tilde{\rho}\rho^\alpha_{\mathrm{e}+}\mathbf{p}^\alpha_0\cdot\mathbf{L}^{\mathrm{p}}\mathbf{p}^\alpha_0\,\mathrm{d}V-\int_V \tilde{\rho}f_{\mathrm{e}}(\rho^\alpha_{\mathrm{s}+}-\rho^\alpha_{\mathrm{s}-})\mathbf{p}^\alpha_0\cdot\mathbf{L}^{\mathrm{p}}\mathbf{m}^\alpha_0\,\mathrm{d}V\\
&+\int_S \tilde{\rho}[\rho^\alpha_{\mathrm{e}+}\bar{v}^\alpha_{\mathrm{e}+}+f_{\mathrm{e}}(\rho^\alpha_{\mathrm{s}+}\bar{v}^\alpha_{\mathrm{s}+}+\rho^\alpha_{\mathrm{s}-}\bar{v}^\alpha_{\mathrm{s}-})](\mathbf{F}^{\mathrm{p}-1}\mathbf{m}^\alpha_0)\cdot\mathbf{n}_{\mathrm{s}}\,\mathrm{d}S, \qquad (32)
\end{aligned}
$$

where S is the surface in the reference configuration with outward normal, $\mathbf{n}_{\mathrm{s}}$, that encloses the volume, V. Eq. (32) can be implemented within a FEM framework, and the constitutive functions specified in the previous section can be evaluated at the volume integration points. In this form, the GND-related terms of the evolution equation are integrated without calculating any directional derivatives of the dislocation density flux, or any gradients of the plastic strain rate. Furthermore, integration of the system of equations shows that additional boundary conditions are needed to complete the boundary value problem when a polarity in the dislocation density is considered.

Dislocation density/density-flux boundary conditions must be specified to solve the dislocation density evolution equations. The additional boundary conditions in the continuum model can be related to the type of dislocation boundary conditions that are applied to discrete dislocation dynamics simulations (Nicola et al., 2003). The density-flux boundary conditions may be placed only on densities whose velocity vector pierces the surface. A dislocation density-flux across a surface may be prescribed to set the rate of plastic deformation associated with that dislocation density on the surface of the deforming volume. A zero dislocation density-flux boundary condition, with a non-zero density at the boundary, is equivalent to bounding the plastically deforming volume by an impenetrable obstacle to dislocation glide.

Conversely, the surface may be prescribed to act as a dislocation density surface source or sink. If a crystal on one side of the boundary surface deforms more easily than the other, it may act as a source of one dislocation density and a sink for other types of dislocation densities in the less deforming grain. Dislocations pile up at grain boundaries as a result of such processes in which one dislocation density becomes abundantly available at the grain boundary while its polar counterpart is absent. The behavior of free surfaces is the extreme limit of this type of behavior in which the vacuum may be considered as a medium with an infinite dislocation mobility such that it acts as a sink for density but not as a source. In the limit, a free surface with such properties would lead to a “zero” dislocation density boundary condition as any dislocation incident on the boundary would be quickly absorbed. The “zero density” and “zero density-flux” boundary conditions are two extremes that internal grain boundaries may exhibit. The behavior of more realistic grain boundaries could be incorporated through mixed dislocation density/density-flux boundary conditions.

The formulation presented here applies to single crystals only. If the deformation behavior of polycrystals is to be modeled using this framework, the essential physics of grain-boundary dislocation density interactions must be incorporated. Grain-boundaries may absorb or transmit incoming dislocations and may emit density, acting as potential sources as well. These processes have been studied numerically using molecular dynamics techniques (de Koning et al., 2002), but not with continuum models. Grain-boundaries in continuum crystal plasticity models have been treated as surfaces of lattice discontinuity, but their interaction with dislocation fluxes crossing them has not been explicitly considered. The finite element implementation of the dislocation density evolution equations allows the interaction of dislocation densities and grain boundaries to be explicitly modeled through dislocation density/density-flux boundary conditions.

If the representative volume element is taken to be large, such that the statistical terms dominate the total evolution of the dislocation density, a valid approximation would be to ignore the components of the evolution equations related to the dislocation flux divergence. Eliminating the flux divergence components from the evolution equations removes the surface term in Eq. (32) and leaves the volumetric terms in the first two lines of the equation. With the removal of the surface term, boundary conditions on the dislocation density/density-flux can no longer be applied. Furthermore, the traction/displacement boundary conditions are the only boundary conditions needed to solve the boundary value problem uniquely, given the approximation of an "all-statistical" dislocation density state within the volume.

4. Example: simple shear of constrained and unconstrained layers

To illustrate the behavior of the model, a series of finite element simulations on a simplified crystal geometry will be conducted. The purpose of the simulations is to demonstrate how the system of equations behaves for a simple system and to evaluate the ability of the model to capture scale-dependent featgres of crystal plasticity resulting from slip inhomogeneity and from different dislocation density/density-flux boundary conditions. The simulations are not intended to represent any real crystalline material, but rather are intended to provide insight as to how the model could reflect the behavior of such materials.

4.1. Example geometry and constitutive equations

A two-dimensional plane-strain idealization of a single crystal will be employed. The idealized crystal geometry is depicted in Fig. 7; it consists of a single slip-system with three dislocation densities: a right-handed edge density, ρ_{e+}; a left-handed edge density, ρ_{e-}; and a screw dipole density, ρ_s. The screw density is quantified only in dipole (non-polar) form because the initial polar screw densities were set equal and the slip-system geometry in the plane-strain idealization restricts the screw density to remain non-polar. The evolution equations in this system of reduced dimensionality become

$$\begin{aligned}\dot{\rho}_{e+} = {} & \frac{\rho_s|\bar{v}_s|}{\bar{l}_s} - \rho_{e+}\rho_{e-}R_e(|\bar{v}_{e+}| + |\bar{v}_{e-}|) \\ & - \frac{\partial}{\partial \mathbf{X}}(\rho_{e+}\bar{v}_{e+} + f_e\rho_s\bar{v}_s)\cdot(\mathbf{F}^{p-1}\mathbf{m}_0), \qquad (33)\end{aligned}$$

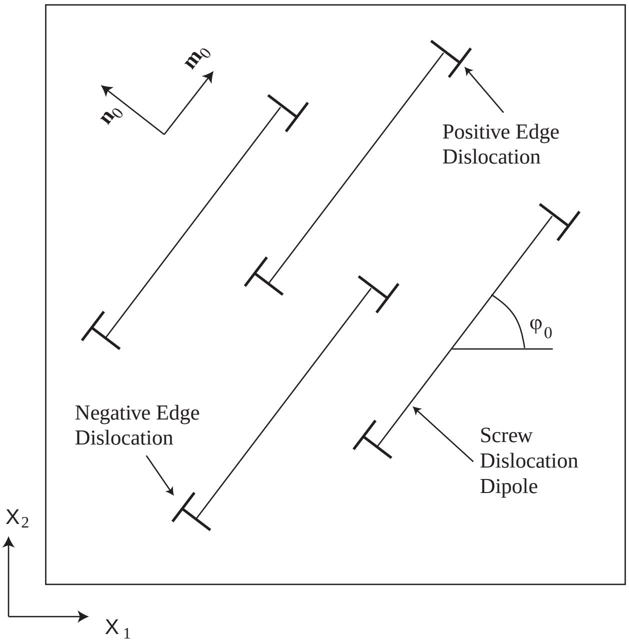

Fig. 7. Dislocation geometry in the reference configuration of the two-dimensional idealized crystal with one-slip-system. The edge dislocations move in the plane of deformation creating screw dislocation dipoles that move in and out of the plane in turn creating edge dislocation dipoles.

$$\begin{aligned}\dot{\rho}_{\mathrm{e}-} = {} & \frac{\rho_{\mathrm{s}}|\bar{v}_{\mathrm{s}}|}{\bar{l}_{\mathrm{s}}} - \rho_{\mathrm{e}+}\rho_{\mathrm{e}-}R_{\mathrm{e}}(|\bar{v}_{\mathrm{e}+}| + |\bar{v}_{\mathrm{e}-}|) \\ & + \frac{\partial}{\partial \mathbf{X}}(\rho_{\mathrm{e}-}\bar{v}_{\mathrm{e}-} + (1 - f_{\mathrm{e}})\rho_{\mathrm{s}}\bar{v}_{\mathrm{s}}) \cdot (\mathbf{F}^{\mathrm{p}^{-1}}\mathbf{m}_0), \end{aligned} \tag{34}$$

$$\dot{\rho}_{\mathrm{s}} = \frac{2\rho_{\mathrm{e}+}|\bar{v}_{\mathrm{e}+}|}{\bar{l}_{\mathrm{e}+}} + \frac{2\rho_{\mathrm{e}-}|\bar{v}_{\mathrm{e}-}|}{\bar{l}_{\mathrm{e}-}} - (\rho_{\mathrm{s}})^2 R_{\mathrm{s}}|\bar{v}_{\mathrm{s}}|. \tag{35}$$

The Burgers vector and the slip plane normal are both in the plane of deformation, and the orientation of the slip-system relative to the global coordinate system is given by the angle φ_0 in the reference configuration. While the edge density glides in the plane of deformation, the screw density glides in and out of the plane. Screw dislocation density has been ignored in other idealized two-dimensional crystal models (Nicola et al., 2003), but in this model, the screw dislocation density is needed to account for the continuing generation of statistical (dipole) edge density, and thus cannot be neglected.

The constitutive functions adopted for the idealized crystal are

$$\bar{v}_{\mathrm{e}+} = \bar{v}_{\mathrm{e}+} = \bar{v}_{\mathrm{s}} = v_0 \left(\frac{|\mathbf{m}_0 \cdot \bar{\mathbf{T}}\mathbf{n}_0 - B|}{c\mu|\mathbf{b}|\sqrt{\rho_{\mathrm{e}+} + \rho_{\mathrm{e}-} + \rho_{\mathrm{s}}}} \right)^{1/m} \operatorname{sign}(\mathbf{m}_0 \cdot \bar{\mathbf{T}}\mathbf{n}_0 - B), \tag{36}$$

$$B = a\mu|\mathbf{b}|\frac{(\mathbf{F}^{\mathrm{p-T}}\,\mathrm{Grad}[\rho_{\mathrm{e+}} - \rho_{\mathrm{e-}}])\cdot\mathbf{m}_0}{\rho_{\mathrm{e+}} + \rho_{\mathrm{e-}}}, \tag{37}$$

$$H_{\mathrm{ee}} = \delta\begin{bmatrix} 1 & 1 \\ 1 & 1 \end{bmatrix}, \tag{38}$$

$$H_{\mathrm{es}} = H_{\mathrm{se}}^{\mathrm{T}} = \delta\begin{bmatrix} 1 \\ 1 \end{bmatrix}, \tag{39}$$

$$H_{\mathrm{ss}} = \delta, \tag{40}$$

$$R_{\mathrm{e}} = R_{\mathrm{s}} = \eta|\mathbf{b}|, \tag{41}$$

$$f_{\mathrm{e}} = 3\left(\frac{\rho_{\mathrm{e+}}}{\rho_{\mathrm{e+}} + \rho_{\mathrm{e-}}}\right)^2 - 2\left(\frac{\rho_{\mathrm{e+}}}{\rho_{\mathrm{e+}} + \rho_{\mathrm{e-}}}\right)^3, \tag{42}$$

where v_0 is a reference velocity, m is the strain rate sensitivity, μ is the isotropic shear modulus, c is the strength associated with dislocation forest interactions, B is the configurational stress, a is the strength coefficient associated with the configurational stress, δ is a constant detailing the amount of loop nucleation occurring during the course of plastic deformation, and η is scaling factor for the capture radii. The values of the material parameters for this idealized crystal may be found in Table 1.

The constitutive form of the stress, B, resolved on the slip plane in Eq. (37) employs a proportional relationship between the stress and the gradient of the dislocation polarity in the slip direction and an inversely proportional relationship with the total edge density. The constitutive form is taken from the work Groma et al. (2003) in which a gradient dependent stress contribution is derived from analysis of dislocation pair correlations in simple two-dimensional discrete dislocation dynamics simulations. The result of their derivation is an internal stress with the same dislocation density dependence as used in Eq. (37). More general forms for these gradient dependent stresses have been

Table 1
Material parameters used for the idealized two-dimensional crystal with a single slip-system

$C_{11} = 108$ GPa
$C_{12} = 61.3$ GPa
$C_{44} = 28.5$ GPa
$\mu = 25.0$ GPa
$v_0 = 1 \times 10^{-9}$ m/s
$m = 0.01$
$c = 0.3$
$a = 0.5$
$\delta = 0.001$
$\eta = 40$
$|\mathbf{b}| = 2.863$ Å

proposed through the framework of Menzel and Steinmann (2000). By associating a free energy of the crystal with tr $(\mathbf{A}^{\mathrm{T}}\mathbf{A})$, Menzel and Steinmann derive a configurational stress tensor that is a function of Curl $(\mathbf{A})$, and work-conjugate to the rate of plastic deformation. The Curl of Nye's tensor is composed of the gradients of polar dislocation densities in directions perpendicular to their tangent line directions, such as the one used in this treatment. A general form of these configurational stresses with the dipolar dislocation density in the denominator has not been proposed, but rather additional material constants with units of length have been considered (Bittencourt et al., 2003).

The system of equations was implemented in ABAQUS/Standard using the user-element interface (ABAQUS, 2003). A generalized bi-linear plane strain element was implemented with five nodal degrees of freedom: two displacement and three density degrees of freedom. A streamline upwinding technique was used to stabilize the convection part of the density evolution equations. As the size of these finite elements decreases, the convective part begins to dominate the dipolar reaction part of the dislocation density evolution equations, and convection-dominated flows are known to be numerically unstable in central difference schemes, as is common in finite element methods. The elements were fully streamline upwinded using the anisotropic diffusion technique described by Brooks and Hughes (1982).

Two different boundary value problems were considered using this idealized crystalline geometry: simple shear of a constrained thin film and simple shear of a thin film with quasi-free surface boundary conditions. A summary of the traction/displacement and dislocation density/density-flux boundary conditions for both of the boundary value problems may be found in Table 2. As discussed in the previous section, the zero surface density boundary condition may be applied to model the limiting behavior of a free surface; however, in the quasi-free surface boundary condition applied here, the dislocation density on the surface is kept constant during the course of the simulation. The boundary condition was applied in this manner so as to not introduce any gradients in the initial dislocation density field. As the simulation proceeded, the constant surface density boundary condition became an increasingly better approximation to the free surface boundary condition as the dislocation density in the interior of the films multiplied by several orders of magnitude.

In both sets of simulations, the slip system was oriented with $\varphi_0 = -90°$ such that the edge dislocation densities move vertically in the unrotated lattice, and a constant shear rate of $\dot{\gamma} = 10^{-3}/\mathrm{s}$ was applied to the layers for 50 s of simulation time, reaching a final shear strain level of 5%. The initial dislocation density distribution in the thin films was homogeneously distributed with $\rho_{\mathrm{e+}} = \rho_{\mathrm{e-}} = 10^{11}\ \mathrm{m}^{-2}$ and $\rho_{\mathrm{s}} = 2 \times 10^{11}\ \mathrm{m}^{-2}$, and a common average segment length of $\bar{l}^{\xi} = 1\ \mu\mathrm{m}$ was assigned to all the initial dislocation densities. Five different thin-film thicknesses were simulated: 3, 10, 30, 100, and 300 μm thick films were considered for each boundary condition case. The element size in each of the simulations was held constant at 100 nm in order to capture any boundary layers that developed in all of the different film thicknesses. The stress/strain behavior of the thin films, the accumulated plastic slip, and the dislocation polarity profiles are investigated to show the overall behavior of the model for these two boundary value problems.

Table 2
A summary of the traction/dislplacement (τ/u) and dislocation density/density-flux ($\rho^{\xi}/\rho^{\xi}\bar{v}^{\xi}$) boundary conditions imposed on the thin films for the simple shear simulations with fixed surfaces and quasi-free surfaces

Fixed surface boundary conditions
$u_1[X_1 = w, X_2, t] = u_1[X_1 = 0, X_2, t]$
$u_2[X_1 = w, X_2, t] = u_2[X_1 = 0, X_2, t]$
$u_1[X_1, X_2 = h, t] = u_1[X_1, X_2 = 0, t] + \dot{\gamma} t$
$\tau_2[X_1, X_2 = h, t] = \tau_2[X_1, X_2 = 0, t] = 0$
$u_1[X_1 = 0, X_2 = 0, t] = 0$
$u_2[X_1 = 0, X_2 = 0, t] = 0$
$\rho_{e+}[X_1 = w, X_2, t] = \rho_{e+}[X_1 = 0, X_2, t]$
$(\rho_{e+}\bar{v}_{e+})[X_1, X_2 = h, t] = (\rho_{e+}\bar{v}_{e+})[X_1, X_2 = 0, t] = 0$
$\rho_{e-}[X_1 = w, X_2, t] = \rho_{e-}[X_1 = 0, X_2, t]$
$(\rho_{e-}\bar{v}_{e-})[X_1, X_2 = h, t] = (\rho_{e-}\bar{v}_{e-})[X_1, X_2 = 0, t] = 0$
$\rho_{s}[X_1 = w, X_2, t] = \rho_{s}[X_1 = 0, X_2, t]$
Quasi-free surface boundary conditions
$\tau_1[X_1 = w, X_2, t] = \tau_1[X_1 = 0, X_2, t] = 0$
$u_2[X_1 = w, X_2, t] = u_2[X_1 = 0, X_2, t]$
$u_1[X_1, X_2 = h, t] = u_1[X_1, X_2 = 0, t] + \dot{\gamma} t$
$\tau_2[X_1, X_2 = h, t] = \tau_2[X_1, X_2 = 0, t] = 0$
$u_1[X_1 = 0, X_2 = 0, t] = 0$
$u_2[X_1 = 0, X_2 = 0, t] = 0$
$\rho_{e+}[X_1 = w, X_2, t] = \rho_{e+}[X_1 = 0, X_2, t]$
$\rho_{e+}[X_1, X_2 = h, t] = \rho_{e+}[X_1, X_2 = 0, t] = \rho_{e+}[X_1, X_2 = 0, t = 0]$
$\rho_{e-}[X_1 = w, X_2, t] = \rho_{e-}[X_1 = 0, X_2, t]$
$\rho_{e-}[X_1, X_2 = h, t] = \rho_{e-}[X_1, X_2 = 0, t] = \rho_{e-}[X_1, X_2 = 0, t = 0]$
$\rho_{s}[X_1 = w, X_2, t] = \rho_{s}[X_1 = 0, X_2, t]$

4.2. Results of thin film simulations

The stress/strain behavior for the constrained thin film with the zero density flux boundary conditions, depicted in Fig. 8, shows a significant length-scale dependence in material response. As the thickness of the film decreases, the strength of the film increases. This is similar to the behavior experimentally observed in thin-wire torsion (Fleck et al., 1994) and micro-beam bending (Stölken and Evans, 1998) in which the normalized strength increases with decreasing specimen size; however, in this mode of deformation, there is no net geometric dislocation content within the layer, in contrast to those deformation modes. The thin film does not deform homogeneously; however, Burgers circuits taken around subsections of the film do yield different net Burgers vectors.

The inhomogeneity of the deformation is depicted in the contour plot of the accumulated plastic slip on the single slip-system found in Fig. 9. In the 3 and 10 μm thick films, the region of the film away from the boundaries plastically deforms more than the regions near the boundary of the film. In the thicker films, the plastic deformation forms a distinct pattern, with a spacing between the shear concentrations on the order of 7.5 μm that remains constant as the thickness of the films increases. In the case of

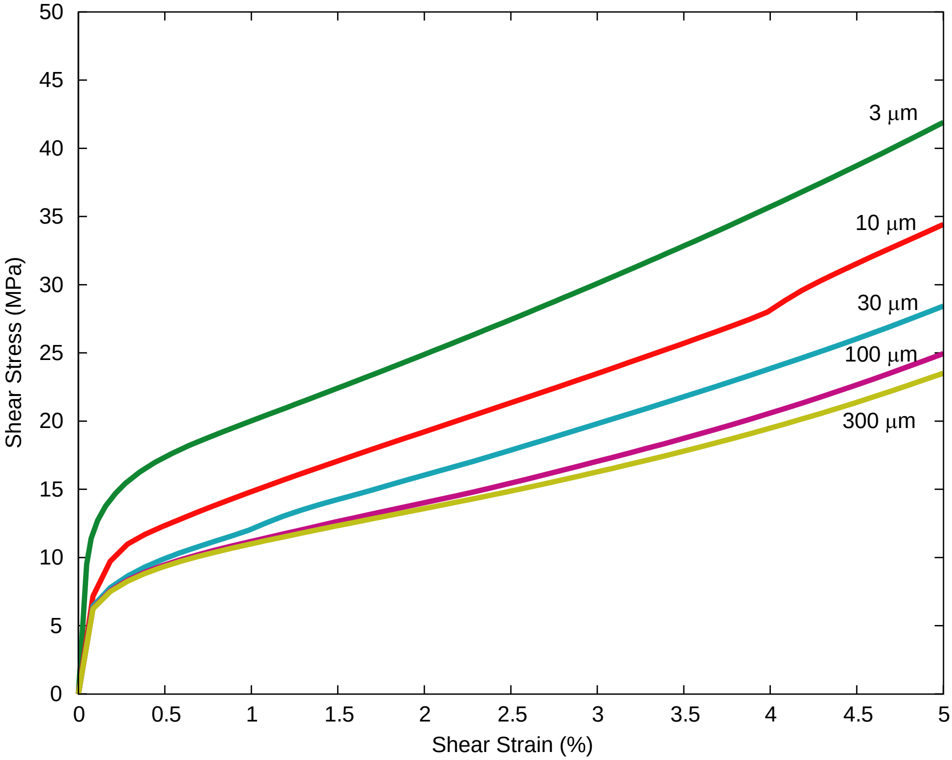

Fig. 8. Thickness-averaged shear stress vs. shear strain curves for simple shear of constrained thin films of an idealized two-dimensional single crystal with one-slip-system for five different film thicknesses.

the 30 μm film, the shear concentration is strongest in the center, and the concentration is strongest in the band closest to the boundary for the thicker films. Differences in the relative position of the strongest shear concentration may be due to the superposition of the heterogeneous boundary layers in the thinner section.

Since the gradients in the plastic deformation occur in the slip direction, a polarity in the dislocation density develops on either side of the shear concentrations. The polarity of the dislocation density for the constrained thin film is given in Fig. 10. The polarity of the density in this simplified one-slip-system model is just the difference between the positive and negative edge densities. With the application of stress and orientation of the slip-system with $\varphi_0 = -90^\circ$, the positive edge dislocation density moves from bottom to top, while the negative edge density moves from top to bottom. As a result, positive edge density piles up against the constrained top surface, while negative edge density piles up against the bottom, in both cases due to the zero dislocation density-flux boundary conditions imposed. The pile-ups are clearly evident in the 3 and 10 μm films, and also appear near the boundaries in the thicker films as well. The thicker sections also develop polarities in the edge density on either side of the plastic

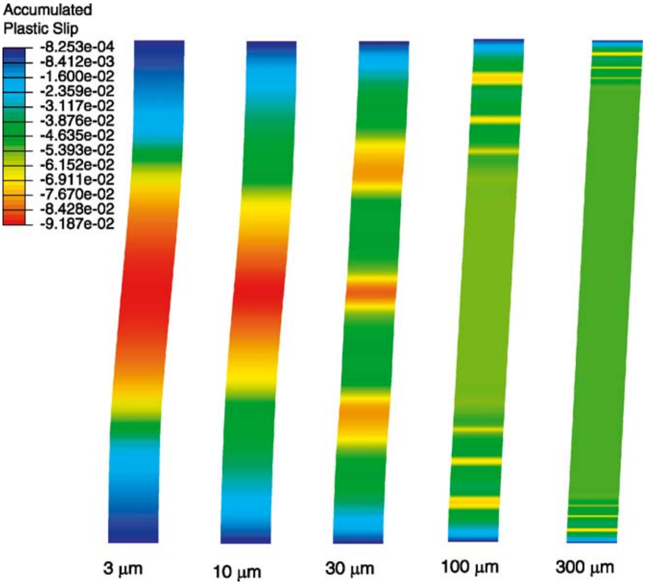

Fig. 9. Contour plots of the accumulated plastic slip for in the constrained thin films for each film thickness, at an average shear strain of 5%.

concentrations, consistent with the flux divergence of the gliding densities. The spacing of the shear concentrations changes during the simulations due to the evolving dislocation density field, and the dependence of the continuing growth of the density and of the configuration stress on that field. Had the single slip-system been oriented with $\varphi_0 = 0$, the gradients of the plastic deformation would have been in the direction of the slip plane normal, and no polarity in the dislocation density would have developed, due to the plastic slip gradients shown in Fig. 9.

The stress/strain behavior of the thin films with the quasi-free surface boundary conditions is shown in Fig. 11 for the five different film thicknesses considered. Unlike the behavior for the constrained film, the stress/strain response for the different thicknesses does not show an appreciable length-scale dependence. Although the different curves do not overlap, the difference in the response is small when compared to the differences observed in the simulations with the constrained surfaces.

The accumulated plastic slip profile for the thin films with quasi-free surfaces on top and bottom, depicted in Fig. 12, shows that deformation is again inhomogeneous. In the 3 μm film, the regions near the surfaces of the thin film plastically deform more than the interior, and in each of the thicker sections, the films have a region of increased slip near the surface. In the thicker films, the deformation in the interior of films shows inhomogeneity in the plastic slip. The shear concentrations again show the same regular spacing of 7.5 μm that was observed in the simulations with constrained boundaries.

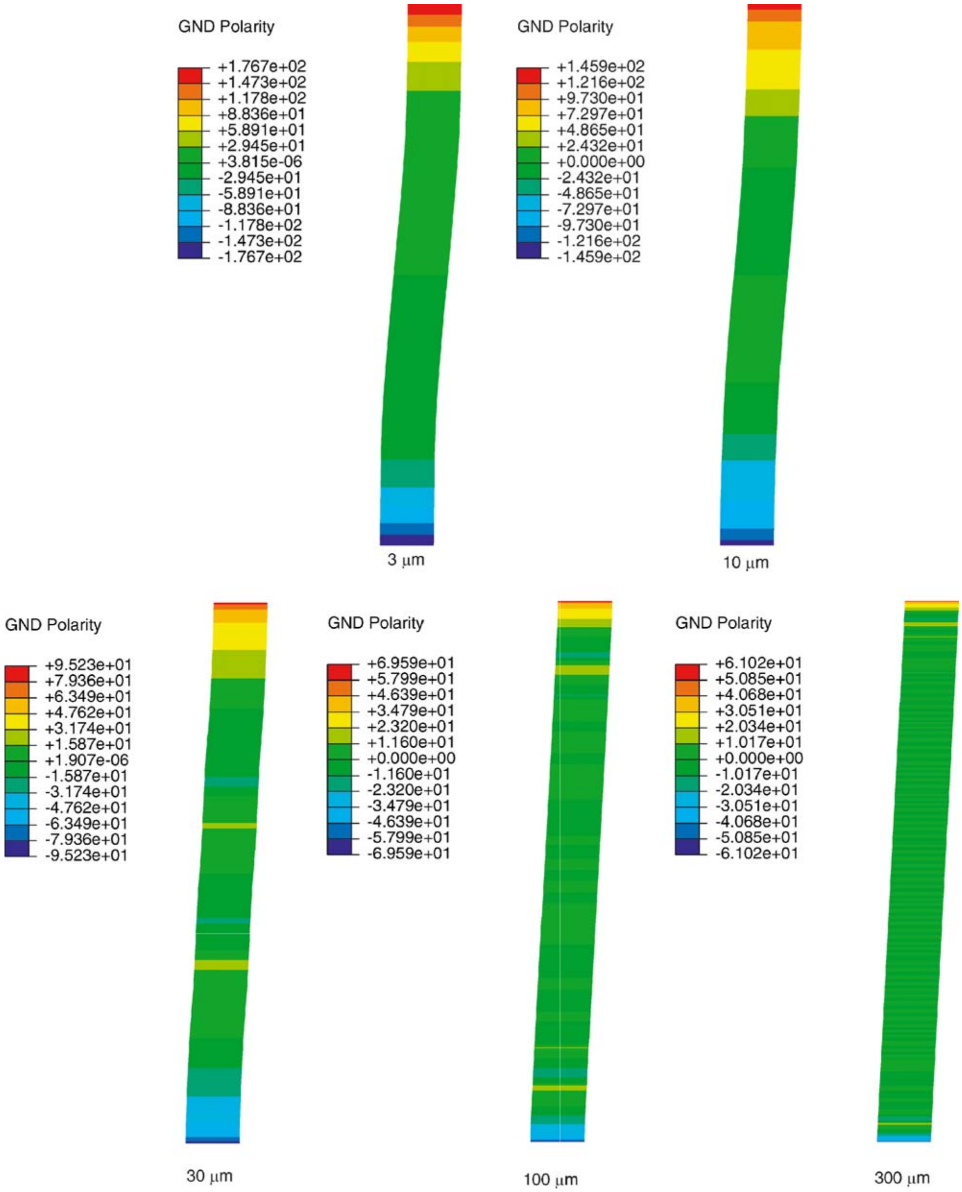

Fig. 10. Contour plots of the polarity of the dislocation density field in the constrained thin films for each film thickness, at an average shear strain of 5%.

The gradients of the plastic slip led to the development of polarity in the dislocation density, as in the previous case. Fig. 13 shows the distribution of the dislocation polarity in the films for each thickness. Unlike the previous case, there are no pileups

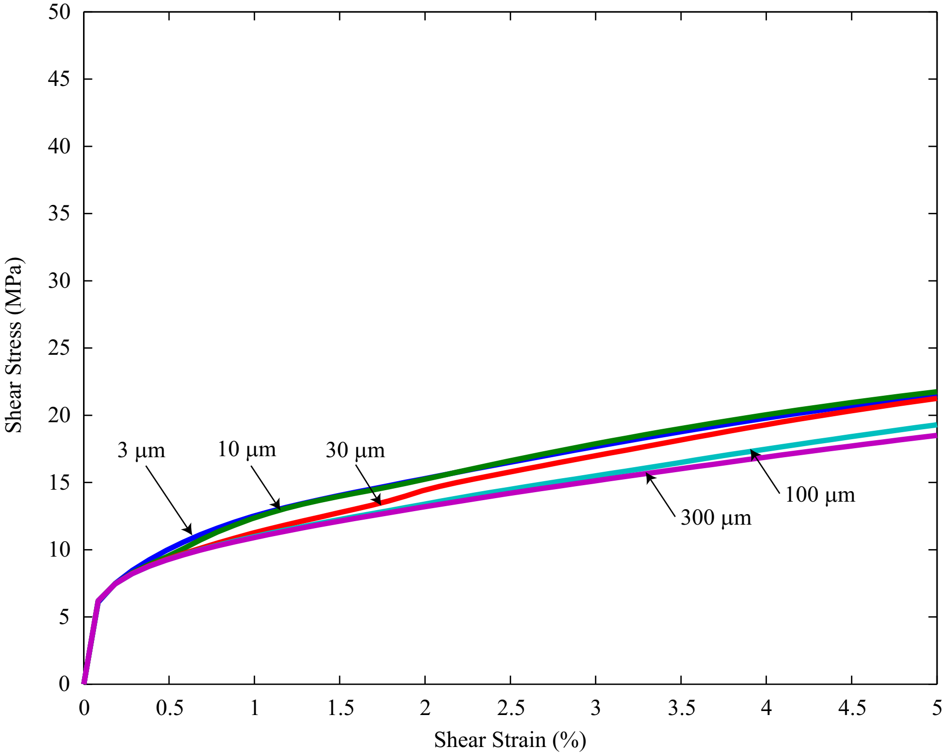

Fig. 11. Thickness-averaged shear stress vs. shear strain curves for simple shear of thin films of an idealized two-dimensional single crystal with one-slip-system and with quasi-free surface boundaries, for five different film thicknesses.

of edge dislocation density at the boundaries. In fact, the polarity of the edge dislocation density at the surfaces is required to be zero, due to the imposed initial boundary and density conditions. Similar to the previous case, a net dislocation polarity was observed on either side of the shear concentrations, consistent with the flux divergence of the dislocation densities. The symmetry of the dislocation polarity contour plots shown in both Figs. 10 and 13 results in no net geometric content in the thin films.

4.3. Discussion

The two sets of simulations have implications as to the net influence of grain boundaries on the strength of deforming polycrystals. The two dislocation density/density-flux boundary conditions applied to the thin films are extremes for the behavior of grain boundaries within a polycrystal. The zero flux boundary condition corresponds to the case when a neighboring grain does not plastically deform, and the quasi-free surface boundary condition corresponds to the case when a neighboring grain deforms to such an extent as to draw dislocation density from its neighbors. The behavior of real grain

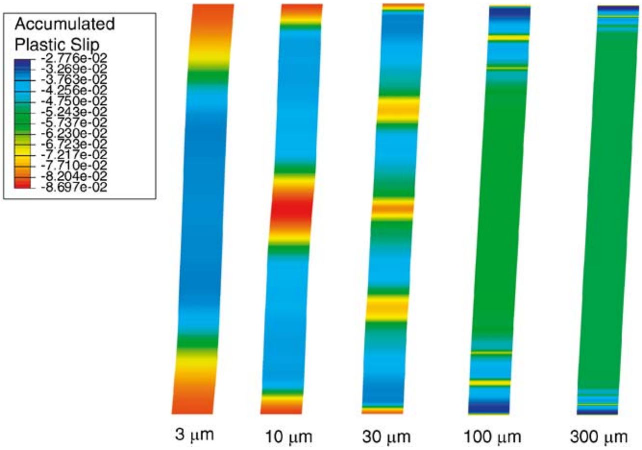

Fig. 12. Contour plots of the accumulated plastic slip in the thin films with quasi-free surface boundaries for each film thickness, at an average shear strain of 5%.

boundaries in a polycrystal will lie somewhere between these two extremes. The constrained thin film was observed to significantly strengthen as the thickness of the film decreased, while the quasi-free surface bounded thin film did not soften, but rather showed very little length scale-dependence in its mechanical response. As a result, the net effect of grain boundaries in a polycrystalline simulation would be to strengthen the response as the grain dimension is decreased.

The strengthening with decreased layer size observed in the simulations results despite the symmetry in the material model and in the simulation geometry because the symmetry is broken by the boundary conditions applied. The scale-dependent material behavior of the model is captured with the evolution of the dislocation polarity and the configurational stress in Eq. (37). Eliminating these two elements from the material model would render the formulation scale independent. The treatment of the evolution of the dislocation polarity is symmetric in that the polar density may either increase or decrease the local total density, depending on the flux divergence of each mobile dislocation species. The configurational stress is also perfectly symmetric and may both augment or decrement the elastic stress, depending on the direction of the density gradients. While other boundary conditions may break the symmetry of the model, leading to a net softening response with decreasing dimension, the symmetry-breaking associated with grain boundaries should strengthen with decreasing dimension, as evidenced in the simple simulations conducted in this example. The magnitude of the change in the material strength with decreasing length scale is proportional to the a-parameter in Eq. (37) that scales the resistance due to gradients in the polarity of the dislocation density.

The simulations conducted were of a geometrically unrealistic crystal, and despite the simplicity of the simulation geometry, interesting heterogeneities developed. Essential elements of the constitutive model should lead to similar behavior for more complex

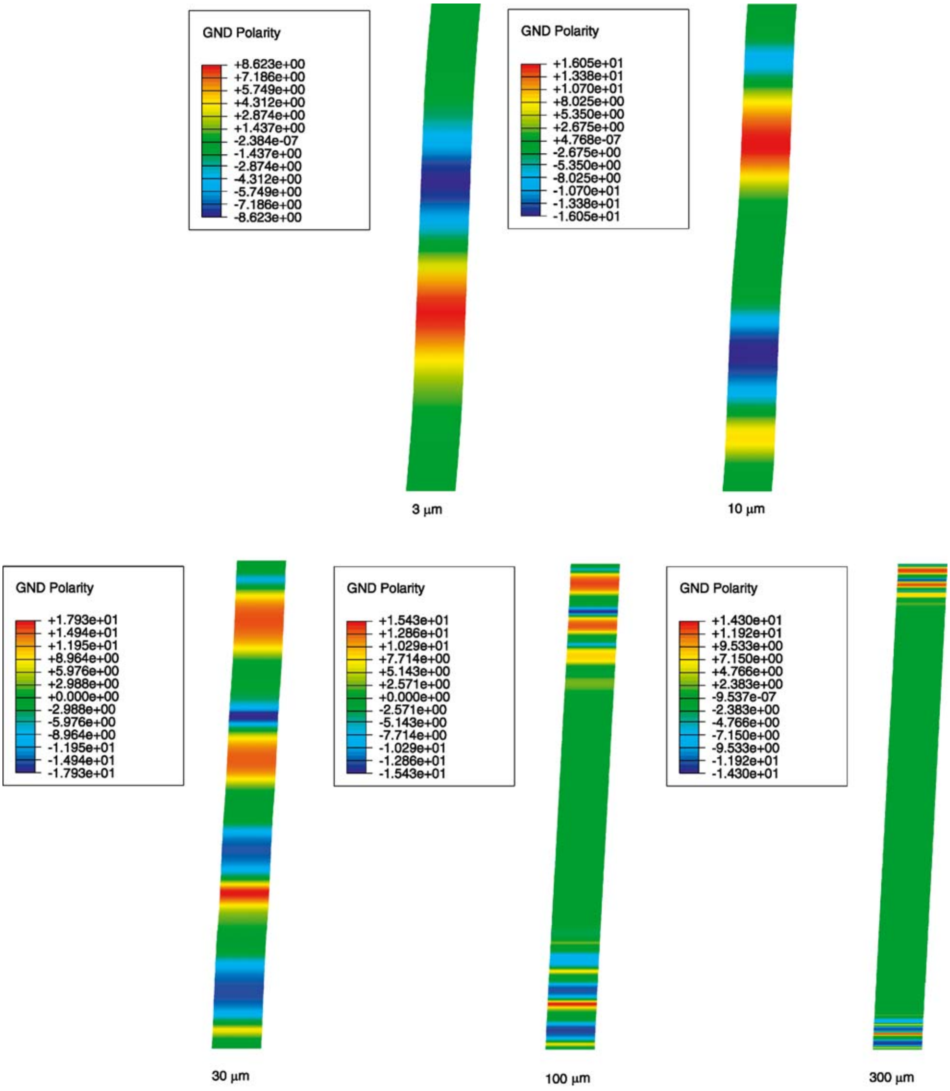

Fig. 13. Contour plots of the polarity of the dislocation density field in the thin films with quasi-free surface boundaries for each film thickness, at an average shear strain of 5%.

two- and three-dimensional polycrystals with multiple slip-systems. The simplicity of this system introduced only three dislocation density nodal degrees of freedom in the finite element implementation. Similar implementation of an fcc crystal would require at least 48 dislocation density nodal degrees of freedom evolving simultaneously. The finite element size could be larger than the 100 nm employed in this example because the boundary layers anticipated from such simulations would be less sharp. Nonetheless, the computational cost of such a simulation would be too great to justify using a model of this complexity and detail in macroscopic calculations. However, the model would be advantageous within a multi-scale modeling framework in bridging the gap between dislocation dynamics simulations and continuum polycrystal plasticity simulations with volume elements containing tens of grains.

5. Conclusion

A dislocation density-based model for continuum crystal plasticity has been formulated that incorporates a material length-scale dependence in its framework. The model is developed such that it can be applied to simulate the behavior of crystals at different length scales by incorporating the spatio-temporal evolution of both statistical and geometric density. The statistical density evolves through generation and annihilation mechanisms. As dislocation line segments glide, new dislocation line segments must be generated to maintain continuity of the dislocation line structure. The rate of growth of the density is proportional to the number density of mobile segments and their to average velocity. The annihilation of density occurs in a net Burgers vector-conserving manner by considering the recombination of polar opposite dislocation densities leaving behind perfect crystal. The rate of density removal is proportional to the two reacting densities, their relative velocity, and a critical distance of self-capture.

The generation and annihilation portions of the general density evolution equations conserve the net Burgers vector of the volume in which they occur; however, the divergence of dislocation density flux leads to a net change in the Burgers vector of the volume. Inhomogeneous plastic deformation may lead to an accumulation or loss of density within the volume, depending on the direction of the gradients of the plastic deformation and the dislocation densities involved. Further homogeneous plastic deformation in a volume that has a non-zero dislocation density tensor may change the value of the density tensor through reactions between the glide density and the geometric forest density.

The integration of the system of equations demonstrated that, in addition to the traction/displacement boundary conditions needed to solve stress equilibrium, dislocation density/density-flux boundary conditions had to be included to solve the dislocation density evolution equations. The additional boundary conditions arose from the flux divergence component of the dislocation density evolution equations, and if the dislocation density was assumed to be completely statistical in nature, approximating the condition in large representative volumes, then the additional dislocation density/density-flux boundary conditions could be ignored.

An idealized two-dimensional crystal with a single slip-system was implemented into a commercial finite element package and used to simulate the mechanical behavior of thin films under conditions of simple shear, with rigid and quasi-free surface boundaries. The simulations showed that the strength of the films with rigid boundaries increased as the thickness of the film decreased while the strength of the films with the quasi-free surface boundary conditions on density did not vary significantly with thickness. The plastic deformation in both sets of simulations was inhomogeneous for all of the different thicknesses, and a regular of spacing of 7.5 μm developed between internal regions of increased slip.

The formulation and the simulations provide guidance as to the explicit modeling of grain boundaries in polycrystalline materials and as to their net effect on the mechanical behavior of the aggregate. The volume integration of the dislocation density evolution equations suggests that grain boundaries could be modeled using surface elements with traction-displacement, dislocation density/density-flux constitutive equations. The influence of grain boundaries on the mechanical response of the aggregate will lie between the two extreme boundary conditions simulated in the simple shear examples. The net effect of the grain boundaries will be to strengthen the polycrystal, and the strength will increase as the grain dimension decreases. Future work will focus on the development of constitutive equations for the interaction of gliding dislocation densities incident on grain boundaries, and on the development of more robust numerical techniques for solving the dislocation density evolution equations.

Acknowledgements

This work was performed under the auspices of the US Department of Energy by the University of California, Lawrence Livermore National Laboratory under Contract No. W-7405-Eng-48. Additional financial support was provided by the National Defense and Engineering Graduate Fellowship Program and by the National Science Foundation under Grant No. 9700358.

References

ABAQUS Inc., 2003. ABAQUS Reference Manuals Version 6.3. Pawtucket, RI.

Acharya, A., 2001. A model of crystal plasticity based on the theory of continuously distributed dislocations. J. Mech. Phys. Solids 49, 761–784.

Acharya, A., Bassani, J.L., 2000. Lattice incompatibility and a gradient theory of crystal plasticity. J. Mech. Phys. Solids 48, 1565–1595.

Acharya, A., Beaudoin, A.J., 2000. Grain-size effect in viscoplastic polycrystals at moderate strains. J. Mech. Phys. Solids 48, 2213–2230.

Arsenlis, A., Parks, D.M., 1999. Crystallographic aspects of geometrically-necessary and statistically-stored dislocation density. Acta Mater. 47, 1597–1611.

Arsenlis, A., Tang, M., 2003. Crystal plasticity continuum model development from dislocation dynamics. Model. Simul. Mater. Sci. Eng. 11, 251–264.

Asaro, R.J., Rice, J.R., 1977. Strain localization in ductile single crystals. J. Mech. Phys. Solids 25, 309–338.

Ashby, M.F., 1970. The deformation of plastically non-homogeneous alloys. Philos. Mag. 21, 399–424.

Bilby, B.A., Bullough, R., Smith, E., 1955. Continuous distributions of dislocations: a new application of methods of non-reimannian geometry. Proc. R. Soc. London A A231, 263.

Bittencourt, E., Needleman, A., Gurtin, M.E., Van der Giessen, E., 2003. A comparison of nonlocal continuum and discrete dislocation plasticity. J. Mech. Phys. Solids 51, 218–310.

Bronkhorst, C.A., Kalidindi, S.R., Anand, L., 1992. Polycrystalline plasticity and the evolution of crystallographic texture in FCC metals. Philos. Trans. R. Soc. London A 341, 443–477.

Brooks, A.N., Hughes, T.J.R., 1982. Streamline upwind/petrov-galerkin formulations for convection dominated flows with particular emphasis on the incompressible Navier-Stokes equations. Comput. Methods Appl. Mech. Eng. 32, 199–259.

Cermelli, P., Gurtin, M.E., 2001. On the characterization of geometrically necessary dislocations in finite plasticity. J. Mech. Phys. Solids 49, 1539–1568.

Cuitiño, A.M., Ortiz, M., 1992. Computational modelling of single crystals. Model. Simul. Mater. Sci. Eng. 1, 225–263.

Dai, H., Parks, D.M., 1997. Geometrically-necessary dislocation density and scale-dependent crystal plasticity. PLASTICITY '97, Proceedings of the Sixth International Symposium on Plasticity and its Current Applications. Juneau, Alaska, pp. 17–18.

de Koning, M., Miller, R., Bulatov, V.V., Abraham, F.F., 2002. Modeling grain-boundary resistance in intergranular dislocation slip transmission. Philos. Mag. 82, 2511–2527.

Fleck, N.A., Hutchinson, J.W., 1997. Strain gradient plasticity. Adv. Appl. Mech. 33, 295–361.

Fleck, N.A., Muller, G.M., Ashby, M.F., Hutchinson, J.W., 1994. Strain gradient plasticity: theory and experiment. Acta Metall. Mater. 42, 475–487.

Follansbee, P.S., Kocks, U.F., 1988. A constitutive description of the deformation of copper based on the use of the mechanical threshold stress as an internal state variable. Acta Metall. Mater. 36, 81–93.

Gao, H., Huang, Y., Nix, W.D., Hutchinson, J.W., 1999. Mechanism-based strain gradient plasticity—I. Theory. J. Mech. Phys. Solids 47, 1239–1263.

Godfrey, A., Hughes, D.A., 2000. Scaling of the spacing of deformation induced dislocation boundaries. Acta Mater. 48, 1897–1905.

Groma, I., Csikor, F.F., Zaiser, M., 2003. Spatial correlations and higher-order gradient terms in a continuum description of dislocation dynamics. Acta Mater. 51, 1271–1281.

Gurtin, M.E., 2002. A gradient theory of single-crystal viscoplasticity that accounts for geometrically necessary dislocations. J. Mech. Phys. Solids 50, 5–32.

Kocks, U.F., 1959. Polyslip in single crystals of face-centered cubic metals. Ph.D. Thesis, Harvard University.

Kröner, E., 1962. Dislocations and continuum mechanics. Appl. Mech. Rev. 15, 599.

Kubin, L.P., Canova, G., Condat, M., Devincre, B., Pontikis, V., Brechet, Y., 1992. Dislocation microstructures and plastic flow: a 3D simulation. Solid State Phenomena 23 & 24, 455–472.

Ma, Q., Clarke, D.R., 1995. Size dependent hardness in silver single crystals. J. Mater. Res. 10, 853–863.

Marin, E.B., Dawson, P.R., 1998. On modelling the elasto-viscoplastic response of metals using polycrystal plasticity. Comput. Methods Appl. Mech. Eng. 165, 1–21.

Menzel, A., Steinmann, P., 2000. On the continuum formulation of higher gradient plasticity for single and polycrystals. J. Mech. Phys. Solids 48, 1777–1796.

Mülhaus, H.B., Aifantis, E.C., 1991. A variational principle for gradient plasticity. Int. J. Solids Struct. 28, 845–857.

Nemat-Nasser, S., Ni, L.Q., Okinaka, T., 1998. A constitutive model for fcc crystals with application to polycrystalline ofhc copper. Mech. Mater. 30, 325–341.

Nicola, L., van der Giessen, E., Needleman, A., 2003. Discrete dislocation analysis of size effects in thin films. J. Appl. Phys. 93, 5920–5928.

Nix, W.D., Gao, H., 1998. Indentation size effects in crystalline materials: a law for strain gradient plasticity. J. Mech. Phys. Solids 46, 411–425.

Nye, J.F., 1953. Some geometrical relations in dislocated crystals. Acta Metall. 1, 153–162.

Ortiz, M., 1999. Plastic yielding as a phase transition. J. Appl. Mech. Trans. ASME 66, 289–298.

Schwartz, A.J., King, W.E., Campbell, G.H., Stölken, J.S., Lassila, D.H., Sun, S., Adams, B.L., 1999. Orientation imaging microscopy investigation of the compression deformation of a [0 1 1] ta single crystal. J. Eng. Mater. Technol. 121, 178–181.

Schwarz, K.W., 1999. Simulation of dislocations on the mesoscopic scale: I. Methods and examples. J. Appl. Phys. 85, 108–119.

Shu, J.Y., Fleck, N., 1999. Strain gradient crystal plasticity: size-dependent deformation of bicrystals. J. Mech. Phys. Solids 47, 297–324.

Sluys, L.J., Estrin, Y., 2000. The analysis of shear banding with a dislocation based gradient plasticity model. Int. J. Solids Struct. 37, 7127–7142.

Smyshlyaev, V.P., Fleck, N., 1996. The role of strain gradients in the grain size effect for polycrystals. J. Mech. Phys. Solids 44, 465–495.

Stainier, L., Cuitiño, A.M., Ortiz, M., 2002. A micromechanical model of hardening, rate sensitivity, and thermal softening in bcc single crystals. J. Mech. Phys. Solids 50, 1511–1545.

Steinmann, P., 1996. Views on multiplicative elastoplasticity and the continuum theory of dislocations. Int. J. Eng. Sci. 34, 1717–1735.

Stelmashenko, N.A., Walls, M.G., Brown, L.M., Milman, Y.V., 1993. Microindentation on W and Mo oriented single crystals: an STM study. Acta Metall. Mater. 41, 2855–2865.

Stölken, J.S., Evans, A.G., 1998. A microbend test for measuring the plasticity length scale. Acta Mater. 48, 5109–5115.

Sun, S., Adams, B.L., King, W.E., 2000. Observations of lattice curvature near the interface of a deformed aluminum bicrystal. Philos. Mag. 80, 9–25.

Walgraef, D., Aifantis, E.C., 1985a. Dislocation patterning in fatigued metals as a result of dynamical instabilities. J. Appl. Phys. 58, 688–691.

Walgraef, D., Aifantis, E.C., 1985b. On the formation and stability of dislocation patterns .3 3-dimensional considerations. Int. J. Eng. Sci. 23, 1365–1372.

Walgraef, D., Aifantis, E.C., 1988. Plastic instabilities, dislocation patterns, and nonequilibrium phenomena. Res. Mech. 23, 161–195.

Wang, Y.U., Jin, Y.M., Cuitino, A.M., Khachaturyan, A.G., 2001. Nanoscale phase field microelasticity theory of dislocations: model and 3d simulations. Acta Mater. 49, 1847–1857.

Zbib, H.M., Rhee, M., Hirth, J.P., 1998. On plastic deformation and the dynamics of 3D dislocations. Int. J. Mech. Sci. 40, 113–127.